ANALYSIS OF THE SIZE EFFECTS ON THE PSEUDOELASTIC BEHAVIOR OF SHAPE MEMORY ALLOY MICRO-PILLARS

An Honors Fellow Thesis

by

EDWIN ALEXANDER PERAZA HERNANDEZ

Submitted to Honors and Undergraduate Research
Texas A&M University
in partial fulfillment of the requirements for the designation as

HONORS UNDERGRADUATE RESEARCH FELLOW

May 2012

Major: Aerospace Engineering

ANALYSIS OF THE SIZE EFFECTS ON THE PSEUDOELASTIC BEHAVIOR OF SHAPE MEMORY ALLOY MICRO-PILLARS

An Honors Fellow Thesis

by

EDWIN ALEXANDER PERAZA HERNANDEZ

Submitted to Honors and Undergraduate Research
Texas A&M University
in partial fulfillment of the requirements for the designation as

HONORS UNDERGRADUATE RESEARCH FELLOW

Approved by:

Research Advisor: Dimitris C. Lagoudas
Associate Director, Honors and Undergraduate Research: Duncan MacKenzie

May 2012

Major: Aerospace Engineering

ABSTRACT

Analysis of the Size Effects on the Pseudoelastic Behavior of Shape Memory Alloy Micro-pillars. (May 2012)

Edwin Alexander Peraza Hernandez
Department of Aerospace Engineering
Texas A&M University

Research Advisor: Dr. Dimitris C. Lagoudas
Department of Aerospace Engineering

Size dependent properties of Shape Memory Alloys (SMAs) in micro and nano scales have gained an increasing attention due to the existing and potential applications of SMAs in microelectromechanical systems (MEMS) and small scale biomedical devices. Such applications exploit the pseudoelastic and shape memory properties of SMAs. In order to enhance the applicability of SMA micro and nano structures, the size dependency of the thermo-elastic behavior of SMAs should be understood. In this study, the dependency of the pseudoelastic behavior of Nickel-Titanium (NiTi) micro-pillars on their diameter was analyzed. Isothermal compression experiments from literature of bulk and micro-pillars were analyzed to determine the critical transformation stresses for different pillar diameters. The analysis of experimental data shows that the critical transformation stresses increase as the micro-pillar average diameter decreases. The relations between the critical transformation stresses and the average pillar diameter were represented using power functions. It was assumed that the elastic modulus and Poisson's ratios of the austenite and martensite phases, the transformation strain

parameters, and the stress influence coefficients were unaffected by the micro-pillar size. Parametric studies were performed using the finite element analysis to find the effects of the taper angle and the aspect ratio on the micro-pillars behavior. Comparisons of the results found from finite element simulations and experiments show that the model accurately predicts the pseudoelastic response of bulk and micro-pillars. The results of the parametric studies show that the hysteresis of the compression response decreases as the taper angle increases. The effect of the micro-pillar diameter on the compression response is less significant for micro-pillars of higher aspect ratios and higher taper angles.

DEDICATION

To my parents Maria Esperanza and Jose Arturo, for always supporting me and motivating me in the pursuit of my dreams.

ACKNOWLEDGMENTS

I would first and foremost like to thank God for all the blessings He has given me. The glory of all my achievements goes to Him.

I want to express my deepest gratitude to Dr. Dimitris Lagoudas, for being my mentor for this honors thesis and for about two years of undergraduate research so far. I want to thank him for giving me a position in his research group, for showing me the career path I want to follow, and for always guide me and motivate me to do the best in every work.

I wish to express my sincere gratitude Dr. Kaushik Das, for also being my mentor and supervisor since I began to work with Dr. Lagoudas' group. I want to thank him for the time spent helping me in my research, and revising my papers and presentations. Thanks to his advice I greatly improved the quality of my papers, presentations, and research.

I want to thank and acknowledge Dr. Parikshith Kumar for coming up with the main idea of the work presented in this thesis. I want to thank Mr. Stephen Oehler, Mr. Brian Lester, Dr. Darren Hartl and the entire Shape Memory Alloy Research Team for their advice in my research and for always being a helpful and friendly group to work with.

I want to thank the National Science Foundation – Nanotechnology Interdisciplinary Research Team (NSF–NIRT) grant for their financial support for this project. I want to

express my greatest gratitude to FEDISAL/FANTEL and the government of my home country El Salvador, for providing me with the Presidential Scholarship; and to LASPAU, for their help and assistance in the administration of the scholarship. Thanks to their support I was able to pursue my undergraduate studies at Texas A&M.

I would like to thank the staff of the Sponsored Student Programs office at Texas A&M University for their help and assistance since the first day I arrived in the USA. I also want to thank the Honors and Undergraduate Research Office staff for their help during the process of the thesis work.

To my family, friends, professors, colleagues, and to everyone who has contributed to my professional development, I want to thank you from the bottom of my heart.

NOMENCLATURE

A	Power function parameter
A_f	Austenitic finish temperature at zero stress
A_s	Austenitic start temperature at zero stress
B	Power function parameter
b	Body forces
b^A	Parameter for polynomial model
b^M	Parameter for polynomial model
c	Specific heat capacity
C	Power function parameter
c^A	Specific heat capacity of austenitic phase
c^M	Specific heat capacity of martensitic phase
C^A	Stress influence coefficient of austenite
C^M	Stress influence coefficient of martensite
D	Average pillar diameter
E^A	Elastic modulus of austenite
E^M	Elastic modulus of martensite
f	Hardening function
F	Reaction force
FIB	Focused ion beam
G	Specific Gibbs free energy

H^{max}	Maximum attainable transformation strain
L	Pillar length
MEMS	Microelectromechanical systems
M_f	Martensitic finish temperature at zero stress
M_s	Martensitic start temperature at zero stress
$\hat{n}$	Unit vector normal to the body surface
r	Radial coordinate
S	Compliance tensor reduced to a scalar for 1-D uniaxial loading
$\boldsymbol{S}$	Compliance tensor
$\boldsymbol{S}^A$	Compliance tensor of austenite
$\boldsymbol{S}^M$	Compliance tensor of martensite
s_0	Specific entropy at reference state
s_0^A	Specific entropy of austenite at reference state
s_0^M	Specific entropy of martensite at reference state
SEM	Scanning electron microscope
SMA	Shape memory alloy
T	Temperature
T_0	Reference temperature
u	Displacement
u_0	Specific internal energy at reference state
u_0^A	Specific internal energy at reference state

u_0^M	Specific internal energy at reference state
u_1	Defined displacement
Y	Critical value for thermodynamic force to cause transformation
z	Distance from origin parallel to the axisymmetric axis
$\boldsymbol{\alpha}$	Thermal expansion coefficient tensor
$\boldsymbol{\alpha}^A$	Thermal expansion coefficient tensor of austenite
$\boldsymbol{\alpha}^M$	Thermal expansion coefficient tensor of martensite
γ	Shear strain
Γ_i	Body surface
ε	Uniaxial total strain
$\boldsymbol{\varepsilon}$	Infinitesimal strain tensor
$\boldsymbol{\varepsilon}^t$	Transformation strain tensor
$\boldsymbol{\varepsilon}^{t-r}$	Transformation strain at the reversal of phase transformation
$\bar{\varepsilon}^{t-r}$	Effective transformation strain at the reversal of phase transformation
θ	Angle in the reference axisymmetric axis
$\boldsymbol{\Lambda}$	Transformation tensor
μ_i	Model parameters for polynomial model
ξ	Total martensitic volume fraction
π	Thermodynamic force conjugated to ξ
ρ	Mass density

σ	Uniaxial stress
$\boldsymbol{\sigma}$	Cauchy stress tensor
σ^{Af}	Completion stress for reverse transformation into austenite
σ^{As}	Initiation stress for reverse transformation into austenite
σ^{Mf}	Completion stress for forward transformation into martensite
σ^{Ms}	Initiation stress for forward transformation into martensite
$\boldsymbol{\sigma}'$	Deviatoric stress tensor
$\bar{\sigma}'$	Mises equivalent effective stress
Φ	Transformation function
Ω	Solid body region

TABLE OF CONTENTS

Page

LIST OF FIGURES

CHAPTER I

INTRODUCTION

A trend showing the need for material multifunctionality in small scale devices has emerged over the last years [1]. This trend is clearly revealed by the intensive amount of research that has been performed in multifunctional materials such as piezoelectrics, magnetostrictives, electrostrictives, thermoelectrics, shape memory polymers, and SMAs [2]. These materials are part of a family of materials called active materials. Active materials exhibit couplings between diverse forms of energy [1]. For instance, SMAs show coupling between mechanical and thermal energies. One distinctive property of SMAs is their reversible solid to solid phase transformation from a high temperature phase known as austenite to a low temperature phase known as martensite, each with a different crystal structure and therefore different properties. This transformation does not occur by diffusion of atoms, but rather by shear lattice distortions [3].

In addition to thermally induced phase transformation, transformation can occur by applying a sufficiently high stress to the material in the austenitic phase. This stress causes a stress-induced transformation from austenite to martensite. If the temperature is sufficiently high so the SMA is completely in the austenite phase at zero stress, the SMA

This thesis follows the style of the *American Institute of Aeronautics and Astronautics Journal*.

transforms back from martensite to austenite upon unloading and shape recovery is observed. This SMA material behavior is called the pseudoelastic effect [3]. A pseudoelastic loading path in the SMA stress-temperature phase diagram is presented in Fig. 1. The stress-strain diagram associated with this pseudoelastic loading path is presented in Fig. 2.

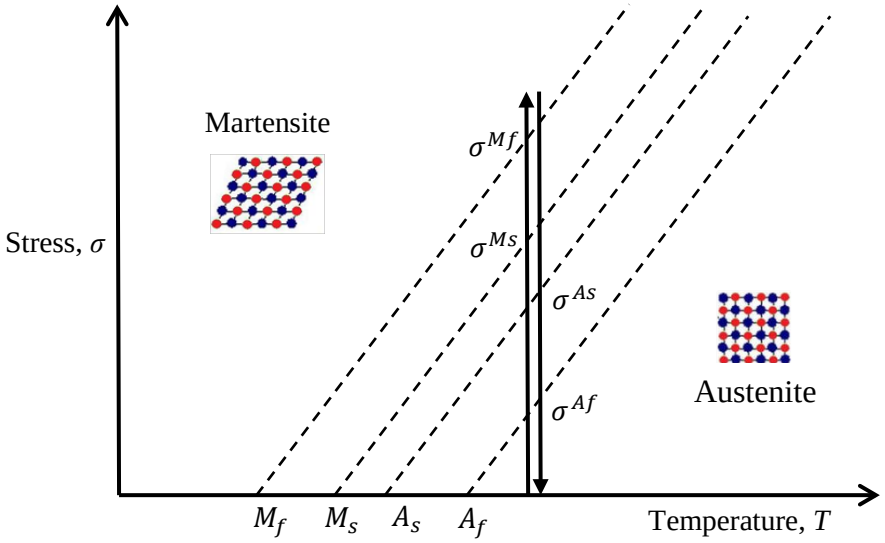

Fig. 1 A pseudoelastic loading path.

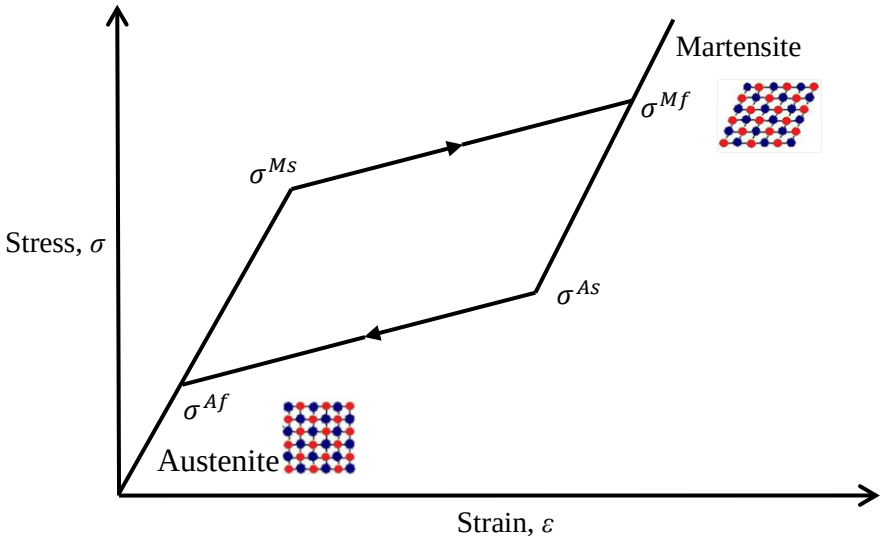

Fig. 2 A pseudoelastic stress-strain diagram.

As the size of SMAs is reduced to the micro and nano scales, it has been found that the material properties exhibit size dependency. Opposite to bulk materials, which material properties are not size dependent, various micro and nano materials show changes in their material properties as their size vary [1]. The dependency of the material properties on the size of the studied specimen is called size effect in this work. Size effects on the thermo-elastic properties of SMAs micro and nano structures have gained an increasing attention due to the existing and potential applications of such structures in MEMS and small scale biomedical devices. In order to enhance the applicability of SMA micro and nano structures, the size effects on their thermo-elastic behavior should be understood.

Applications of SMAs in small scale devices already exist in various MEMS in form of thin films, mostly due to their actuation capabilities [4 – 9]. Such shape memory alloy thin films have been mainly fabricated by sputtering, and exhibit both pseudoelastic and

shape memory properties [10, 11]. Although such films have thicknesses below 15 μm, the essential properties of shape memory effect and pseudoelasticity have been utilized in applications using their largest dimensions above the millimeter size [12]. Therefore, there are several questions about the size effects on the thermo-mechanical behavior of SMAs at small scales that remain unanswered.

Characterization of the thermo-mechanical properties of SMA micro and nano structures represents many challenges due to the extremely small dimensions of the materials. The widely used techniques for characterization of small scale materials are mechanical resonant methods [13], atomic force microscope based methods [14] and nanoindenter based methods (used either as indenter or uniaxial compression device) [15, 16]. The following sections provide a literature review of previous studies in the size effects of SMAs and the objectives of this research.

Literature review of size effects on SMA behavior

The efforts of explaining size effects in SMA behavior at small scales can be abridged under two categories: constrained and non-constrained structures. Constrained structures are in their majority particles and thin films embedded in a matrix. Unconstrained structures include free-standing micro and nano wires, particles, compression pillars, etc.

Among the size effects found in SMA behavior in constrained structures, it can be mentioned the suppression of martensitic phase transformation in NiTi thin films below

~50 nm thickness found by electrical resistivity measurements [17] and mechanical testing [18]. It was suggested that the chemical composition of the film was altered and the phase transformation was restricted by the formation of surface oxide interfacial diffusion layers [18]. Also, spatial constrains by the film surface and the film/substrate interface beget incompatibilities between the martensite and austenite phase that eventually hinder the lattice distortion and twinning [17].

Thermally induced martensitic phase transformation of nanocrystalline NiTi was shown to be completely suppressed for nano-grains with characteristic length below 60 nm [19], and it was revealed a (001) compound twinning behavior for grains between 60 and 100 nm [20]. It was also reported that NiTi films up to 10 μm thickness demonstrate lower transformation temperatures than bulk NiTi of same chemical composition [21]. A significant decrease in martensitic transformation strain was observed for NiTi films with 500 nm thickness as compared to thicker films [22]. NiTiCu nanoparticles embedded in an amorphous matrix revealed the presence of a critical size for suppression of martensitic transformation. It was reported that the transformed nanocrystal volume reduced as the size of the crystal decreased and the martensitic phase transformation was fully suppressed at a critical size of less than 16 nm [23]. Contradicting other previously mentioned experiment results, no significant difference in the thermo-mechanical behavior of Ni-Ti-Cu shape memory films with ~1 μm thickness and bulk was found by substrate-curvature measurements [24].

Studies performed in non-constrained structures also demonstrated size effects in the SMAs thermo-mechanical behavior. Free-standing AuCd nanoparticles were observed to retain bulk-like martensitic transformation temperatures when their size is ~46 nm but showed a lower transformation temperature once their sizes are down to 6 nm [25]. Transmission electron microscope studies on free-standing In-Tl nanowires reported that no size effect is present in temperature induced phase transformation within the diameter range of 650-10 nm [1]. NiTi nanopowders also presented thermally-induced martensitic phase transformation in an average crystal size of ~50 nm [26].

Studies in compression pillars have been performed to determine the size effects on pseudoelasticity and shape memory effect. Pseudoelasticity was observed in NiTi pillars with diameters between 2 μm and 400 nm. It was observed that pseudoelasticity was no longer present for pillars with diameters below 200 nm [27, 28]. Compression pillars made of CuNiAl in the size range between 900 nm and 1.6 μm presented pseudoelastic behavior and shape memory effect in bending pillars with 300 nm and 1.8 μm diameters [29, 30]. It was shown in such studies that there is a significant size effect in the critical phase transformation stresses and stress hysteresis. Such size effects are similar to the ones presented in studies of deformation in metals and metal systems, where it is shown that the materials become stiffer or stronger (e. g. their elastic modulus or yield strength increases, respectively) when their sizes become smaller, usually down to micro and nano scales [31–38].

Research objectives and outline

The two main objectives of this research are to model the size effects on the critical transformation stresses of single crystal NiTi (50.9 at% Ni) micro-pillars and to perform parametric studies using the model to find the effects of aspect ratio and taper angle on the pseudoelastic behavior of such pillars. The studied micro-pillars were fabricated using focused ion beam (FIB) machining. In this method, small scale pillars are created from thin films by removing material from the film until obtain the desired pillar size and shape. An advantage of this technique is that it provides freedom to create micro-pillars of different sizes. Further information about FIB machining can be found elsewhere [39–46]. The geometric parameters of the pillar used in this work are depicted in Fig. 3.

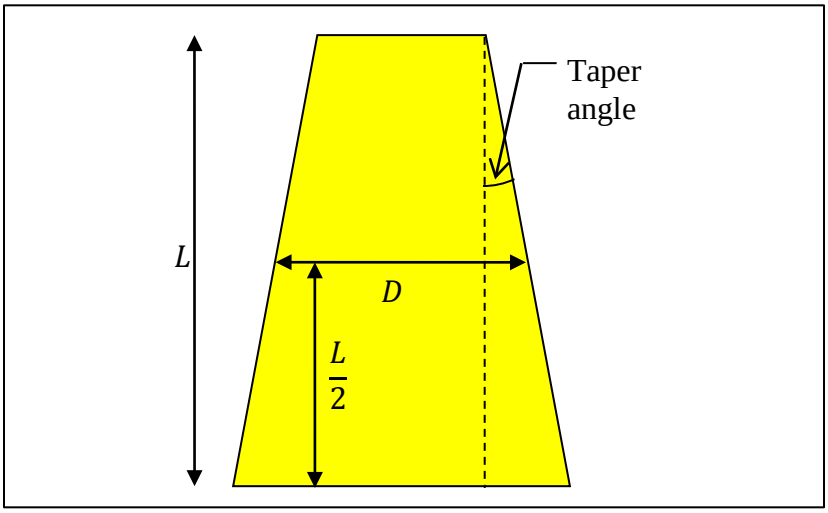

Fig. 3 Geometric parameters of a pillar.

The studied uniaxial compression experiments in the micro-pillars were performed using a nanoindenter. Similar compression experiments in micro-pillars with the objective of

determine size effects were also performed in the past [47–50]. Isothermal compression tests in NiTi bulk and micro-pillars from literature will be analyzed to find the critical transformation stresses for different pillar sizes. Figure 4 shows the SEM picture of the micro-pillar and the geometry used in the finite element analysis is presented in Fig. 5. The geometry of the substrate below the micro-pillars was obtained from scanning electron microscopy (SEM) images provided in literature (Frick, C. P., Orso, S., and Artz, E., "Loss of pseudoelasticity in nickel-titanium sub-micron compression pillars," *Acta Materialia*, Vol. 55, Issue 11, 2007, pp. 3845–3855 [28]). For simplicity, the curved surface of the substrate was modeled as a planar surface. A fillet curve was created at the root of the micro-pillars to avoid effects of sharp corners in the compression response. It was observed from the SEM images of micro-pillars that the root of the micro-pillar is indeed curved and not sharp. The applied displacement pattern and location are presented in Fig. 6.

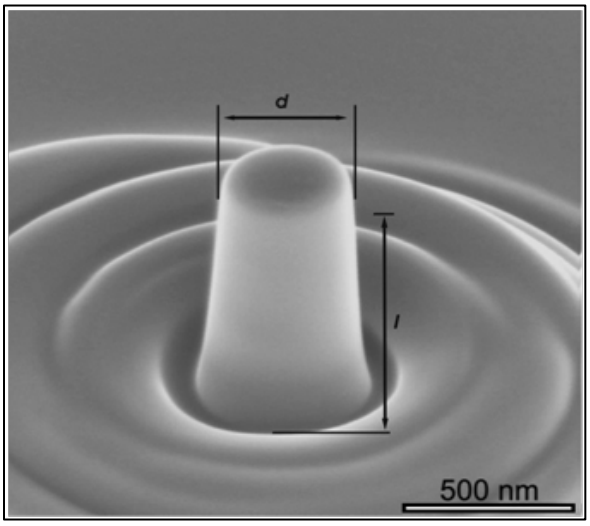

Fig. 4 SEM image of a micro-pillar [28].

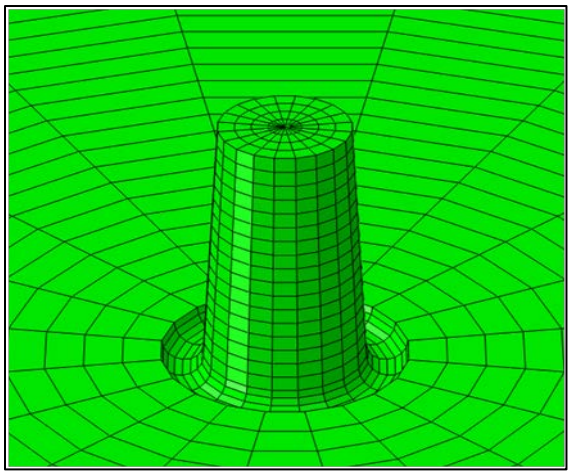

Fig. 5 Geometry of a pillar in finite element simulation.

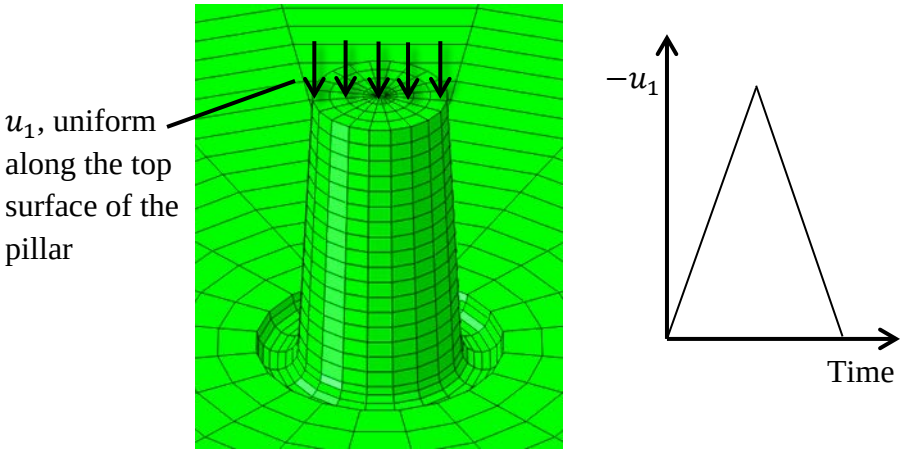

Fig. 6 Applied displacement location and pattern.

The average diameter of the pillars will be used as their characteristic size. Power functions will be used to describe the relations between each of the critical transformation stresses and the average pillar diameter. The model will be implemented in finite element simulations using ABAQUS. A user-defined material model will be implemented in ABAQUS by a user subroutine. It is assumed that the elastic modulus and Poisson's ratios of the austenite and martensite phases, the transformation strain

parameters, and the stress influence coefficients are unaffected by the micro-pillar size. The transformation stresses will be dependent on the micro-pillar diameter. The material properties will be assigned along the micro-pillar by dividing the micro-pillar into several sections along its length. Each section will have the transformation temperatures corresponding to the section average diameter. The parametric studies will consist in simulations of compression test of pillars with different average diameter, aspect ratio, and taper angle. The aspect ratio of the pillar is defined in this work as the total length of the pillar divided by its average diameter.

CHAPTER II

METHODS

Problem description

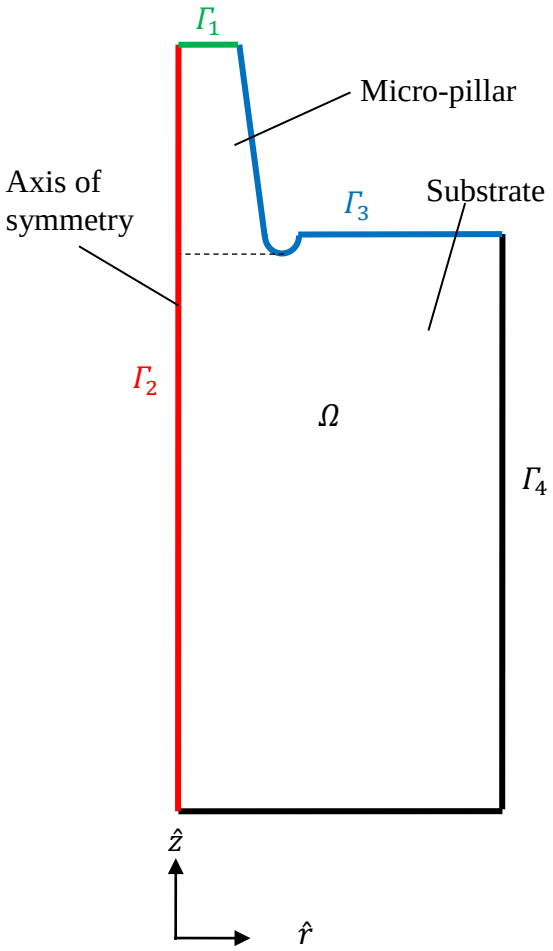

Fig. 7 Geometry of solid body Ω.

The micro-pillar geometry is presented in Fig. 7. Here, the micro-pillar and the substrate are included in the solid body region Ω. The compression experiments were considered as axisymmetric problems due to the axisymmetry of geometry, boundary conditions and

material properties along the long axis of the pillar. The substrate height was selected as about three times the height of the pillar, and the length in the radial direction of the substrate was about three times the diameter of the pillar for all the simulations.

Equilibrium equations

The general 3-dimensional differential equations of linear momentum equilibrium in cylindrical coordinates are presented in Eqs. (1) – (3). The equilibrium equations are valid along the entire solid body Ω.

$$\frac{1}{r}\frac{\partial}{\partial r}(r\sigma_{rr}) + \frac{1}{r}\frac{\partial}{\partial \theta}(\sigma_{r\theta}) + \frac{\partial}{\partial z}\sigma_{rz} - \frac{\sigma_{\theta\theta}}{r} + b_r = 0 \quad (1)$$

$$\frac{1}{r}\frac{\partial}{\partial r}(r\sigma_{zr}) + \frac{1}{r}\sigma_{z\theta} + \frac{\partial}{\partial z}\sigma_{zz} + b_z = 0 \quad (2)$$

$$\frac{1}{r^2}\frac{\partial}{\partial r}(r^2\sigma_{\theta r}) + \frac{1}{r}\frac{\partial}{\partial \theta}(\sigma_{\theta\theta}) + \frac{\partial}{\partial z}\sigma_{\theta z} + b_\theta = 0 \quad (3)$$

For an axisymmetric problem these equations reduce to

$$\frac{1}{r}\frac{\partial}{\partial r}(r\sigma_{rr}) + \frac{\partial}{\partial z}\sigma_{rz} - \frac{\sigma_{\theta\theta}}{r} + b_r = 0 \quad (4)$$

$$\frac{1}{r}\frac{\partial}{\partial r}(r\sigma_{zr}) + \frac{\partial}{\partial z}\sigma_{zz} + b_z = 0 \quad (5)$$

Boundary conditions

The bottom and the outside boundary of the substrate were fixed. The compression experiments were simulated by applying a uniform displacement u_1 at the top surface of the pillar in many steps and measuring the reaction force for each step. Such boundary conditions are defined by the following equations

$$u_z = u_1, \text{ on } \Gamma_1 \tag{6}$$

$$u_r = 0, \text{ on } \Gamma_2 \tag{7}$$

$$\boldsymbol{\sigma} \cdot \hat{n} = 0, \text{ on } \Gamma_3 \tag{8}$$

$$u_r = u_z = 0, \text{ on } \Gamma_4 \tag{9}$$

Constitutive relation

The SMA material behavior analyzed in this study is called the pseudoelastic effect [3]. In addition to thermally induced phase transformation, transformation can occur by applying a sufficiently high stress to the material in the austenitic phase. This results in a stress-induced transformation from austenite to martensite. If the temperature is sufficiently high so the SMA is completely in the austenite phase at zero stress, the SMA transforms back from martensite to austenite upon unloading and shape recovery is observed. In order to capture such material behavior, a constitutive model for SMAs was required.

The constitutive model for SMAs used in this problem has been presented in detail by Lagoudas et al [3]. In this model, the Gibbs free energy is selected to be the thermodynamic potential. The Gibbs free energy is a function of the independent state variable stress $\boldsymbol{\sigma}$, temperature T, and the state variables ξ and $\boldsymbol{\varepsilon}$. The total Gibbs free energy is given by

$$G(\boldsymbol{\sigma}, T, \xi, \boldsymbol{\varepsilon}^t) = -\frac{1}{2\rho}\boldsymbol{\sigma}:\boldsymbol{S}:\boldsymbol{\sigma} - \frac{1}{\rho}\boldsymbol{\sigma}:[\boldsymbol{\alpha}(T - T_0) + \boldsymbol{\varepsilon}^t] +$$

$$c\left[(T - T_0) - T\ln\left(\frac{T}{T_0}\right)\right] - s_0 T + u_0 + \frac{1}{\rho}f(\xi) \tag{10}$$

The material parameters $\boldsymbol{S}$, $\boldsymbol{\alpha}$, c, s_0, and u_0 are the effective compliance tensor, the thermal expansion tensor, the effective specific heat, the effective specific entropy at the reference state, and the effective specific internal energy at the reference state, respectively. The function $f(\xi)$ is a transformation hardening function. The material parameters are defined using the rule of mixtures as

$$\boldsymbol{S} = \boldsymbol{S}^A + \xi(\boldsymbol{S}^M - \boldsymbol{S}^A) \tag{11}$$

$$\boldsymbol{\alpha} = \boldsymbol{\alpha}^A + \xi(\boldsymbol{\alpha}^M - \boldsymbol{\alpha}^A) \tag{12}$$

$$c = c^A + \xi(c^M - c^A) \tag{13}$$

$$s_0 = s_0^A + \xi(s_0^M - s_0^A) \tag{14}$$

$$u_0 = u_0^A + \xi(u_0^M - u_0^A) \tag{15}$$

The total strain is given by

$$\boldsymbol{\varepsilon} = \boldsymbol{S}:\boldsymbol{\sigma} + \boldsymbol{\alpha}(T - T_0) + \boldsymbol{\varepsilon}^t \tag{16}$$

In this model, it is assumed that any change in the current microstructural state of the material is strictly a result of a change in the martensitic volume fraction [3]. Given this assumption, the relation between the transformation strain tensor and the martensitic volume fraction is expressed by

$$\dot{\boldsymbol{\varepsilon}}^t = \boldsymbol{\Lambda}\dot{\xi} \tag{17}$$

Where $\boldsymbol{\Lambda}$ is the transformation tensor, which determines the transformation strain direction. Two different forms of $\boldsymbol{\Lambda}$ are implemented

$$\boldsymbol{\Lambda} = \begin{cases} \frac{3}{2} H^{max} \frac{\boldsymbol{\sigma}'}{\bar{\sigma}'}, & \dot{\xi} > 0 \\ H^{max} \frac{\boldsymbol{\varepsilon}^{t-r}}{\bar{\varepsilon}^{t-r}}, & \dot{\xi} < 0 \end{cases} \tag{18}$$

The deviatoric stress tensor, $\boldsymbol{\sigma}'$, the effective (von Mises equivalent) stress, $\bar{\sigma}'$, and the effective transformation strain at the reversal of the phase transformation, $\bar{\varepsilon}^{t-r}$, are given by

$$\boldsymbol{\sigma}' = \boldsymbol{\sigma} - \frac{1}{3}\mathrm{tr}(\boldsymbol{\sigma})\mathbf{1} \tag{19}$$

$$\bar{\sigma}' = \sqrt{\frac{3}{2}\|\boldsymbol{\sigma}'\|^2} \tag{20}$$

$$\bar{\varepsilon}^{t-r} = \sqrt{\frac{2}{3}\|\boldsymbol{\varepsilon}^{t-r}\|^2} \tag{21}$$

It can be shown [3] that by substituting Eq. (17) into the Clausius-Planck inequality one obtain

$$\left(\boldsymbol{\sigma}:\boldsymbol{\Lambda} - \rho\frac{\partial G}{\partial \xi}\right)\dot{\xi} = \pi\dot{\xi} \geq 0 \tag{22}$$

Where π is the general thermodynamic force conjugated to ξ and is given by

$$\pi = \boldsymbol{\sigma}:\boldsymbol{\Lambda} + \frac{1}{2}\boldsymbol{\sigma}:\Delta\boldsymbol{S}:\boldsymbol{\sigma} + \Delta\boldsymbol{\alpha}:\boldsymbol{\sigma}(T - T_0) -$$

$$\rho\Delta c\left[(T - T_0) - T\ln\left(\frac{T}{T_0}\right)\right] + \rho\Delta s_0 T - \rho\Delta u_0 - \frac{\partial f}{\partial \xi} \tag{23}$$

Where the prefix Δ indicates the difference of a quantity between the martensitic and austenitic phases. Certain assumptions for the forward and reverse transformation [3] allow it to be captured by introducing a transformation function given by

$$\Phi = \begin{cases} \pi - Y, & \dot{\xi} > 0 \\ -\pi - Y, & \dot{\xi} < 0 \end{cases} \tag{24}$$

Constraints on the evolution of the martensitic volume fraction are expressed in terms of the Kuhn-Tucker conditions as

$$\dot{\xi} \geq 0, \quad \Phi = \pi - Y \leq 0, \quad \Phi\dot{\xi} = 0$$

$$\dot{\xi} \leq 0, \quad \Phi = -\pi - Y \leq 0, \quad \Phi\dot{\xi} = 0 \tag{25}$$

The hardening function used in this study was the one provided by the constitutive model presented by Boyd and Lagoudas [3] and it is given by

$$f(\xi) = \begin{cases} \frac{1}{2}\rho b^M \xi^2 + (\mu_1 + \mu_2)\xi, & \dot{\xi} > 0 \\ \frac{1}{2}\rho b^A \xi^2 + (\mu_1 - \mu_2)\xi, & \dot{\xi} < 0 \end{cases} \tag{26}$$

The material parameters b^M, b^A, μ_1, and μ_2 are model parameters that can be determined experimentally. These parameters, along with Y are defined in the quadratic polynomial hardening function model [3] as

$$Y = \frac{1}{4}\rho\Delta s_0\left(M_s + M_f - A_f - A_s\right) \tag{27}$$

$$b^A = -\Delta s_0^A\left(A_f - A_s\right) \tag{28}$$

$$b^M = -\Delta s_0^M\left(M_s - M_f\right) \tag{29}$$

$$\mu_1 = \frac{1}{2}\rho\Delta s_0\left(M_s + A_f\right) - \rho\Delta u_0 \tag{30}$$

$$\mu_2 = \frac{1}{4}\rho\Delta s_0\left(A_s - M_f - A_f + M_s\right) \tag{31}$$

Literature data from bulk NiTi with the same stoichiometry and similar crystallography of the studied micro-pillars were used to obtain the transformation strain parameters, the

elastic modulus of the austenite and martensite phases, the stress influence coefficients, and the stress-strain pseudoelastic response of bulk NiTi [51–54]. Only pseudoelastic experiments where clear transformation was observed and plasticity effects were not significantly high were utilized for this study. Micro-pillars of average diameters of approximately 2135 nm, 1900 nm, and 450 nm were studied [28]. The approximate micro-pillars average diameters were calculated from the geometric parameters provided in the source. In order to find the critical transformation stresses from the stress-strain pseudoelastic responses, straight lines were drawn along the elastic and transformation regions. The stresses at the intersections of these lines were assumed to be the critical transformation stresses. Figure 8 show the line drawing in NiTi with the critical transformation stresses at the intersections of the lines.

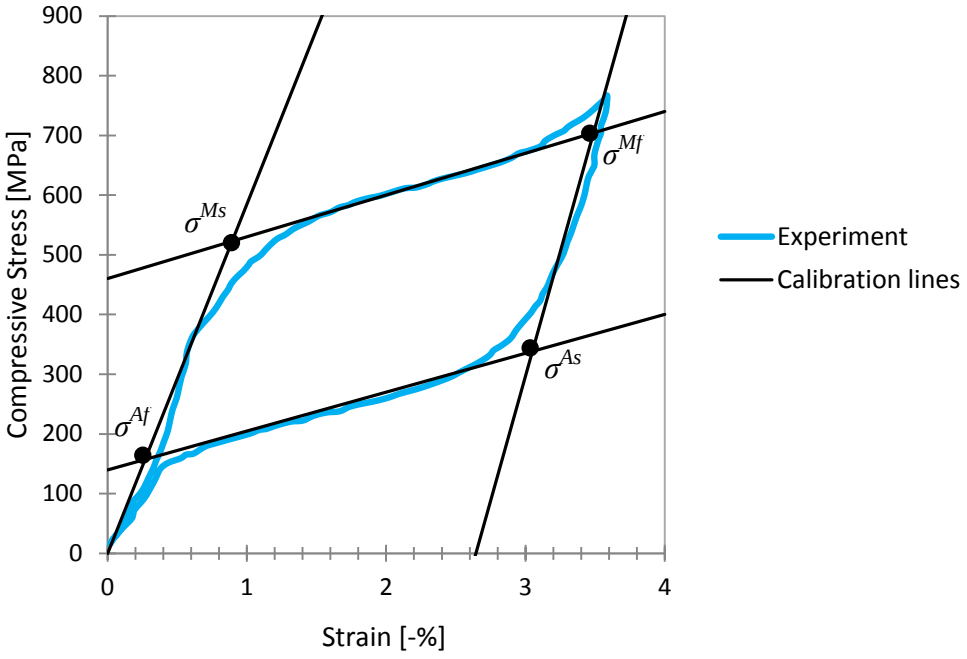

Fig. 8 Bulk NiTi pseudoelastic response [54] with calibration lines.

The previous step allowed for determination of the critical transformation stresses for different pillar diameters. Power functions of the form of Eq. (32) were used to model the four critical transformation stresses as functions of the average pillar diameters.

$$\sigma^{Mf} = AD^B + C \tag{32}$$

Where the parameters A, B and C are found by fitting a power curve into the critical transformation stress vs. average pillar diameter data. Each of the critical transformation stresses has different values for those parameters. Since the simulated experiments are isothermal, T is equal T_0 for all cases, this assumption allows $\boldsymbol{\alpha}$ and c not be needed for this study. In order to fully define the required material parameters of the SMA, some parameters needed to be found. These parameters are the change of specific entropy of austenite at reference state Δs_0^A, the change of specific entropy of martensite at reference state Δs_0^M, and the change in the compliance tensor due to transformation $\Delta \boldsymbol{S}$. For the 1-dimensional case of uniaxial loading of an SMA cylindrical pillar along its long axis, the stress tensor has only one non-zero component. Due to the fact that the stress tensor has one non-zero component for the 1-D compression case, the fourth-order compliance tensor can be reduced to a scalar *S*. The material parameters Δs_0^A, Δs_0^M, and ΔS can be found by solving the following equations

$$\rho \Delta s_0^A = -H^{max} C^A \tag{33}$$

$$\rho \Delta s_0^M = -H^{max} C^M \tag{34}$$

$$\Delta S = \frac{1}{2}\left(\frac{1}{E^M} - \frac{1}{E^A}\right) \tag{35}$$

Here, the stress influence coefficients C^A and C^M are the stress influence coefficients of austenite and martensite, respectively. Once those values are defined, the transformation temperatures at zero stress are given by the following equations

$$\frac{1}{2}\Delta S(\sigma^{Ms})^2 + \sigma^{Ms}H^{max} + \rho\Delta s_0^M(T - M_s) = 0 \quad (36)$$

$$\frac{1}{2}\Delta S(\sigma^{Mf})^2 + \sigma^{Mf}H^{max} + \rho\Delta s_0^M(T - M_s) - \rho b^M = 0 \quad (37)$$

$$\frac{1}{2}\Delta S(\sigma^{Af})^2 + \sigma^{Af}H^{max} + \rho\Delta s_0^A(T - A_f) = 0 \quad (38)$$

$$\frac{1}{2}\Delta S(\sigma^{As})^2 + \sigma^{As}H^{max} + \rho\Delta s_0^A\left(T - A_f\right) - \rho b^A = 0 \quad (39)$$

At this point, the nine equations (27) – (31) and (36) – (39) have nine unknowns, the four transformation temperatures at zero stress and the model parameters Y, b^M, b^A, μ_1, and μ_2. Those equations can be solved to find all the required parameters that define the SMA constitutive behavior. As shown in Eq. (32), the SMA parameters are dependent on D. It was assumed that the size effect of the pillar diameter only affects the transformation stresses and temperatures while E^A, E^M, C^A, C^M and the transformation strain parameters are size independent. Plasticity was not taken into account in the model. The transformation temperatures of the substrate were assumed to be those of bulk. Each micro-pillar was assigned with the transformation temperatures corresponding to their diameter. In cases where the diameter was not constant the micro-pillar was divided into ten sections along its long dimension as shown in Fig. 9. Each section was assigned the transformation temperatures corresponding to its average diameter. The substrate was assumed to have the properties of bulk SMA.

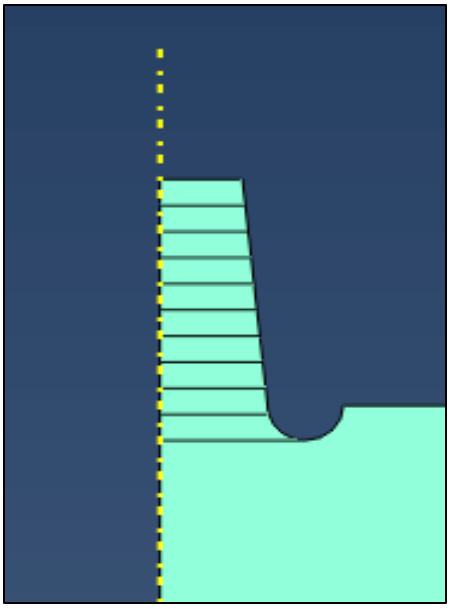

Fig. 9 Micro-pillar divided into sections along its long dimension.

Kinematic equations

The strain-displacement equations for the axisymmetric problem given by the following equations

$$\varepsilon_{rr} = \frac{\partial u_r}{\partial r} \tag{40}$$

$$\varepsilon_{zz} = \frac{\partial u_z}{\partial z} \tag{41}$$

$$\varepsilon_{\theta\theta} = \frac{u_r}{r} \tag{42}$$

$$\gamma_{rz} = \frac{\partial u_r}{\partial z} + \frac{\partial u_z}{\partial r} = \varepsilon_{rz} + \varepsilon_{zr} = 2\varepsilon_{rz} \tag{43}$$

The boundary value problem was solved using ABAQUS finite element analysis software. The following section provides a description of the finite element simulations.

Finite element analysis

Once the material properties of the SMA were defined for different micro-pillar sizes using the previous model, the compression experiments from literature were simulated using the finite element analysis. The finite element mesh for the simulations is presented in Fig. 10.

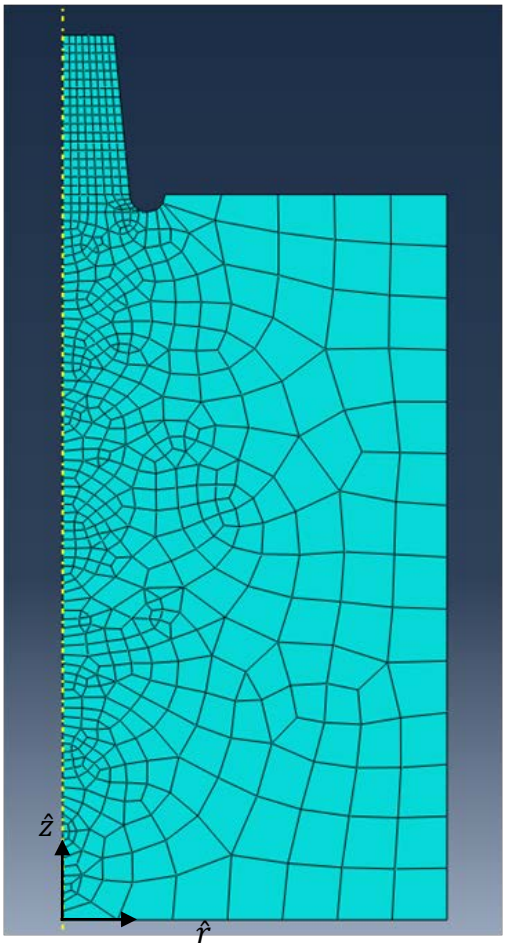

Fig 10. Micro-pillar and substrate finite element mesh.

Simulating the experiments from literature was needed to verify whether the model captures the SMA thermo-elastic behavior and the studied size effect. To simulate the

compression experiments from literature, pillars with constant diameter were used. The diameter of the each simulated pillar corresponded to the average diameter of the experiments. In order to compare the results from the simulation with the stress-strain experimental data the force-displacement output from the finite element analysis was converted into stress-strain using Eq. (44) and Eq. (45).

$$\sigma = \frac{4F}{\pi D^2} \tag{44}$$

$$\varepsilon = \frac{u_1}{L} \tag{45}$$

For the parametric studies, the average pillar diameter, aspect ratio and taper angle were varied. Pillars with average diameters of 500 nm, 2000 nm and 5000 nm were simulated. It is expected that the critical transformation stresses would be more sensible to a slight change in diameter as the pillar diameter decreases due to the non-linear behavior introduced by the critical transformation stresses-diameter power function. The studied aspect ratios were 1.5, 3 and 5. Simulation of micro-pillars with higher aspect ratios may be unrealistic since experimental micro-pillars of high aspect ratios usually experience buckling due to their own weight [28]. The studied taper angles were 0°, 4° and 10°. The material properties of the SMA were inputted in ABAQUS using a user material subroutine. Details of the implementation of the user material subroutine for shape memory alloy modeling have been provided by several authors in the past [56–59]. Figure 11 shows the parametric studies test matrix.

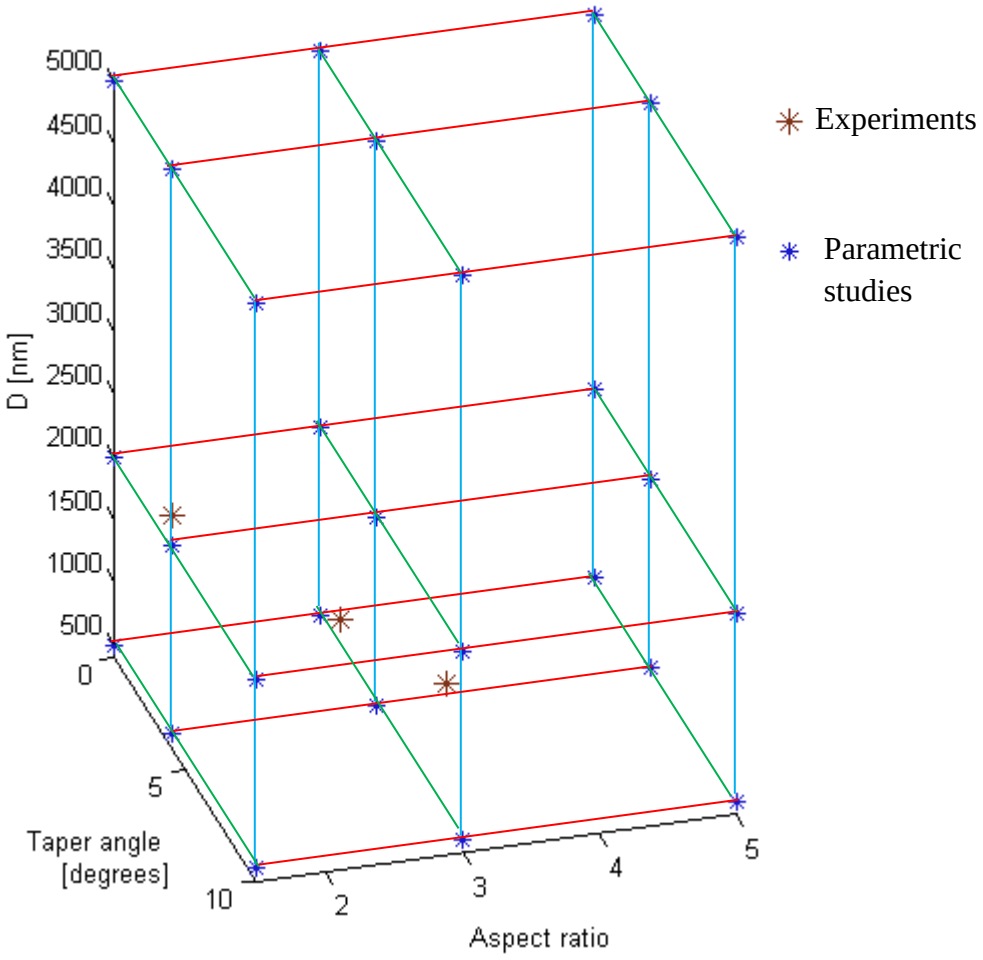

Fig 11. Parametric studies test matrix.

CHAPTER III

RESULTS

Figure 12 shows the critical transformation stresses of the experiments from literature plotted vs. the average pillar diameter. Figure 13 shows a closed view of Fig. 12 for the specific range of studied diameters in the case studies. The power functions used to model the critical transformation stresses are also presented. The power function parameters A, B and C are presented in Table 1. It is observable that all four critical transformation stresses increase as the average pillar diameter decreases. The power fits captured the bulk and 450 nm diameter's transformation stresses with good accuracy, but the 2135 nm and 1900 nm diameter's transformation stresses were not accurately fitted for σ^{As}, σ^{Ms} and σ^{Mf}. The reason is that the fit could not pass through those points because they were very close in diameter (relative to the studied range of diameters) but had a significant difference between their transformation stresses.

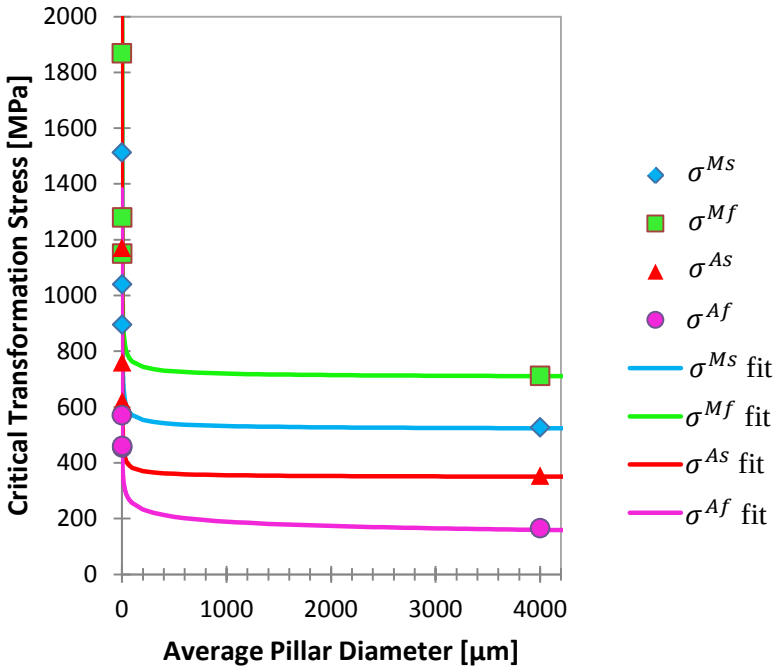

Fig. 12 Critical transformation stresses vs. average pillar diameter.

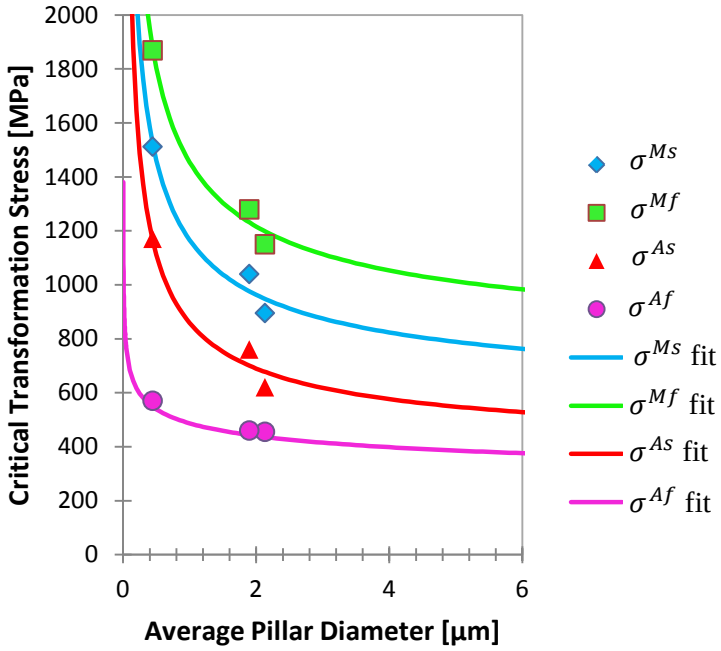

Fig. 13 Critical transformation stresses for small pillar diameters.

Table 1 Power function parameters.

Critical Transformation Stress	A	B	C
σ^{Af}	466.0	–0.1593	40.69
σ^{As}	521.6	–0.5774	346.2
σ^{Ms}	649.4	–0.5408	516.6
σ^{Mf}	751.2	–0.5510	703.2

To illustrate the size effect on the overall thermo-elastic material behavior, the stress-temperature phase diagrams of bulk, a pillar of 1000 nm diameter, and a pillar of 500 nm diameter are presented. Figure 14 shows the martensite transformation lines and Fig. 15 shows the austenite transformation lines. In those figures, the shift in transformation temperatures due to the size effect is observed. According to the presented model, the transformation temperatures at zero stress decrease as the pillar diameter decrease. This decrease in transformation temperatures at zero stress as the average pillar diameter decreases allows the SMA to have higher critical transformation stresses at room temperature.

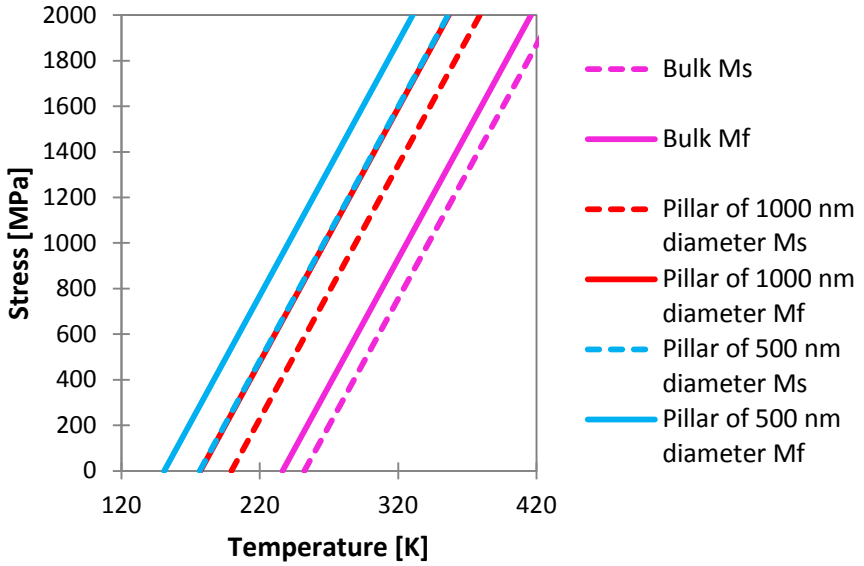

Fig. 14 Stress-temperature phase diagram with transformation to martensite boundaries for different pillar diameters.

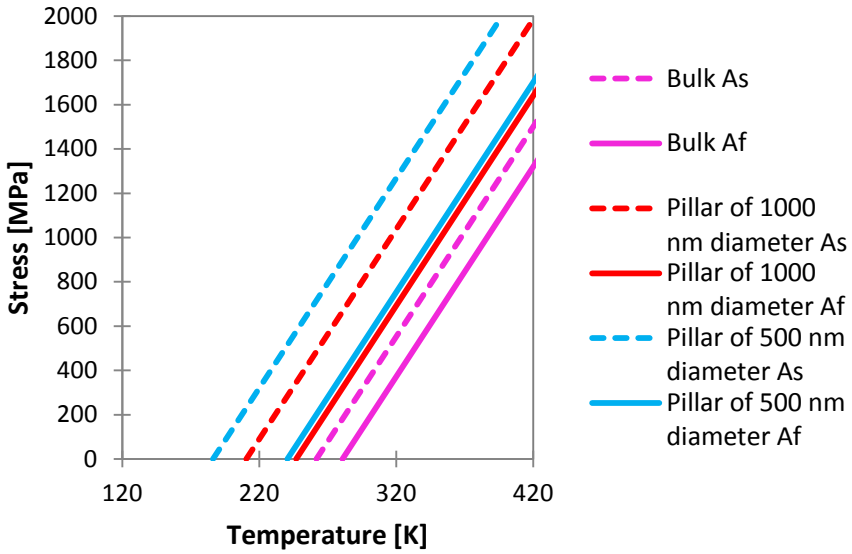

Fig. 15 Stress-temperature phase diagram with transformation to austenite boundaries for different pillar diameters.

Figures 16 – 19 show the results of the finite element simulation plotted with the experimental data. The simulated compression response captured the experimental data with an acceptable accuracy. As expected σ^{As}, σ^{Ms} and σ^{Mf} do not seem to exactly match the experimental data for the pillars of 2135 nm and 1900 nm, this was due to the discrepancies between the estimated transformation stresses and the power fits.

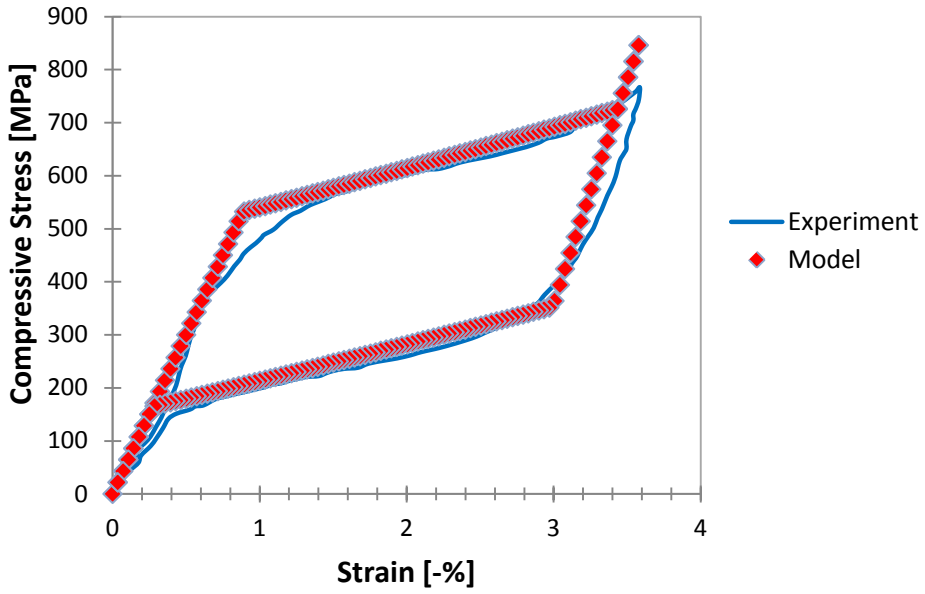

Fig. 16 Comparison of experimental [54] and simulated responses for bulk pillar.

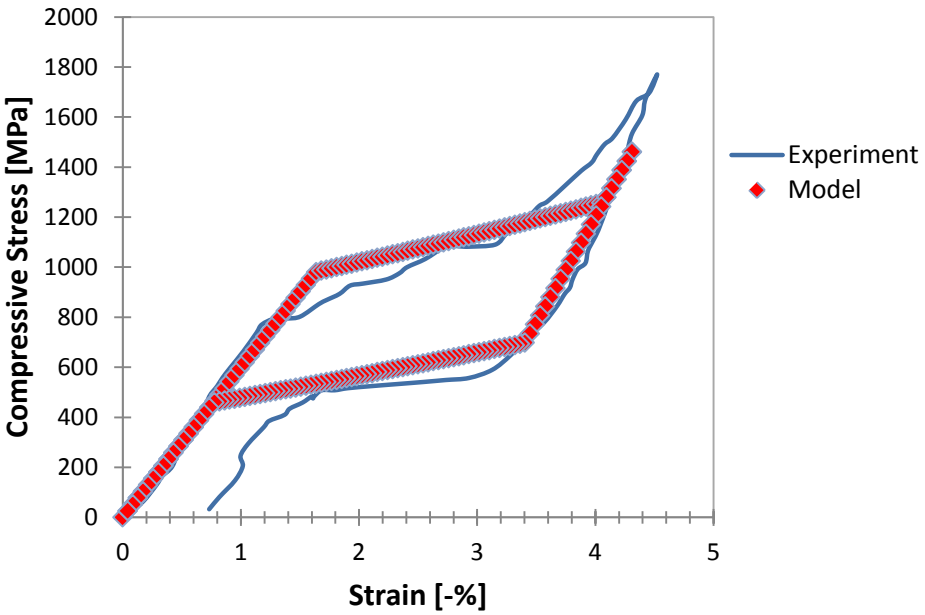

Fig. 17 Comparison of experimental [28] and simulated responses for pillar of ~2135 nm diameter.

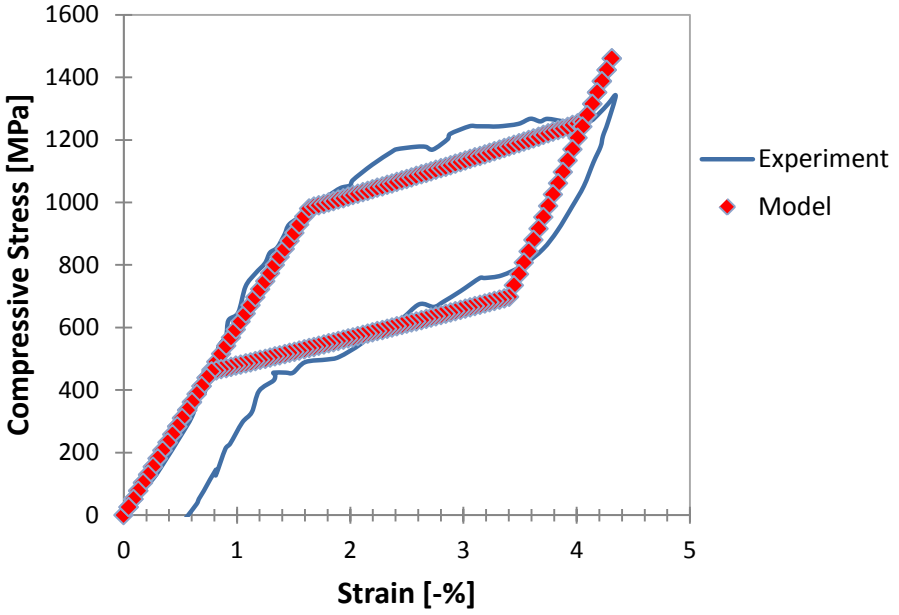

Fig. 18 Comparison of experimental [28] and simulated responses for pillar of ~1900 nm diameter.

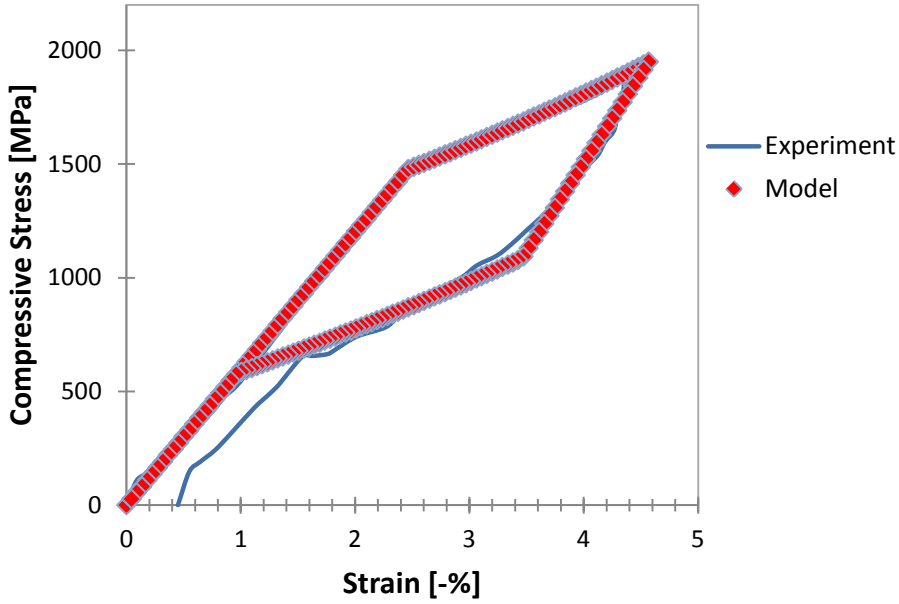

Fig. 19 Comparison of experimental [28] and simulated responses for pillar of ~450 nm diameter.

As stated in the previous chapter. Parametric studies were performed by simulating compression tests in micro-pillars of different diameter, aspect ratio, and taper angle.

First, the effects of taper angle were studied. Figures 20–28 show the results of pillars of 500, 2000, and 5000 nm average diameters with aspect ratios of 1.5, 3 and 5.

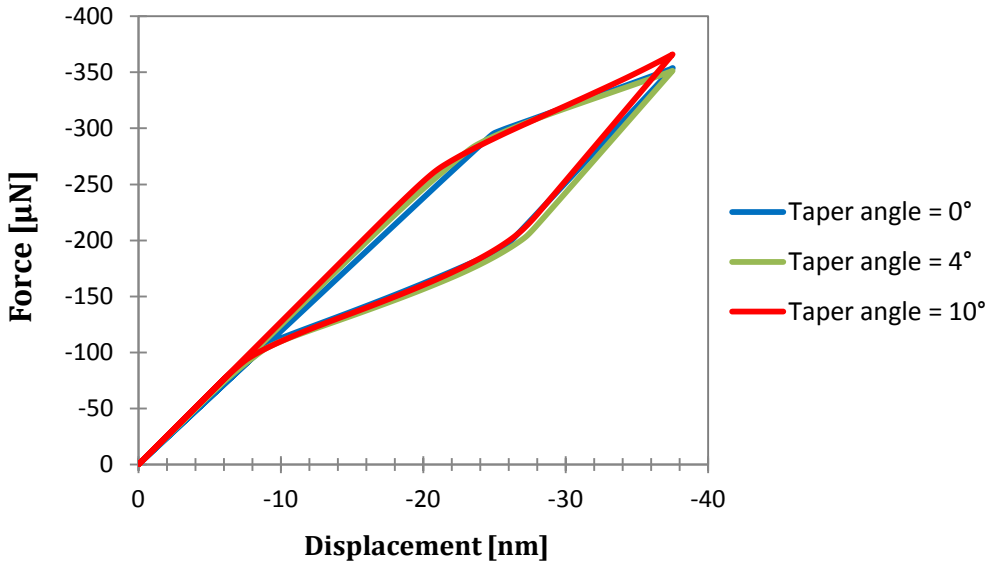

Fig. 20 Force vs. displacement for micro-pillars with average diameter of 500 nm and aspect ratio of 1.5.

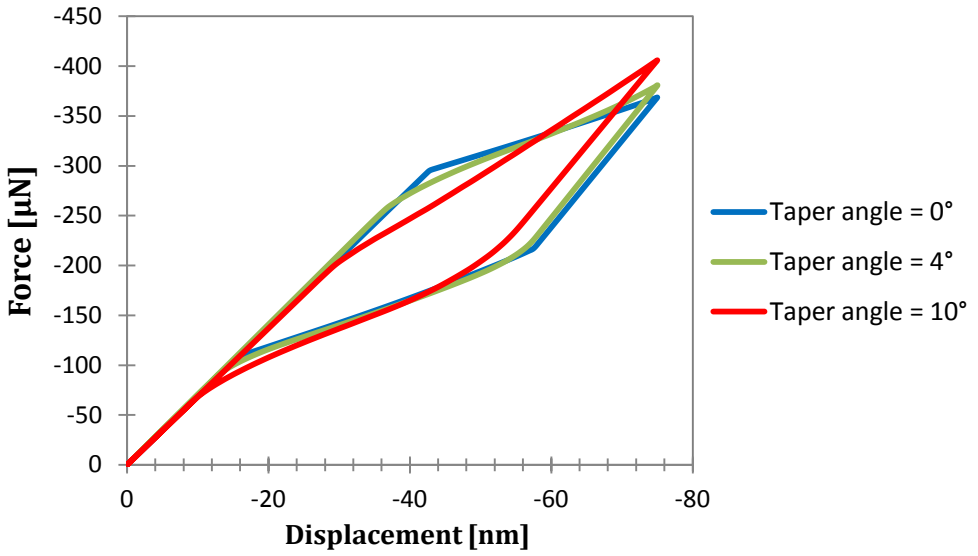

Fig. 21 Force vs. displacement for micro-pillars with average diameter of 500 nm and aspect ratio of 3.

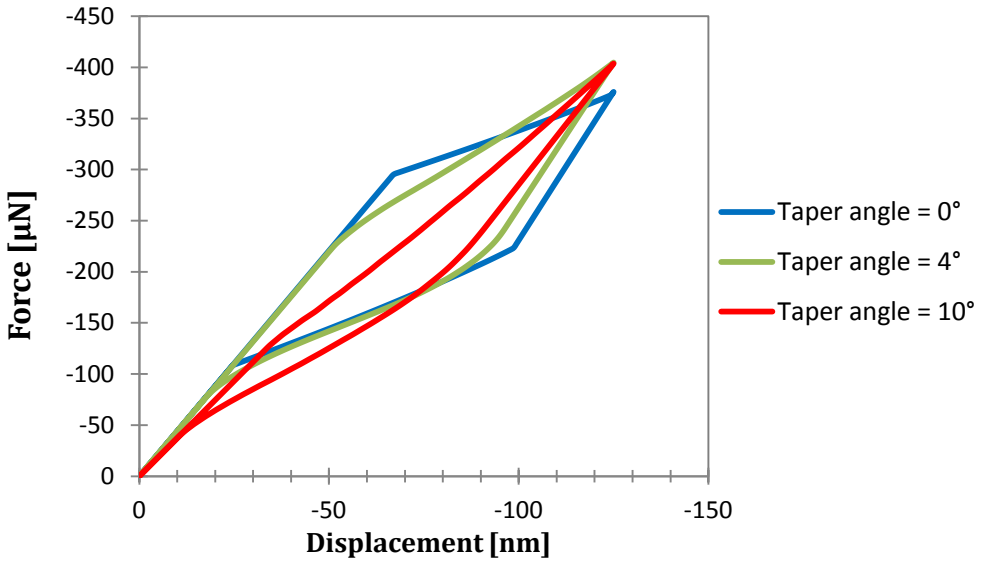

Fig. 22 Force vs. displacement for micro-pillars with average diameter of 500 nm and aspect ratio of 5.

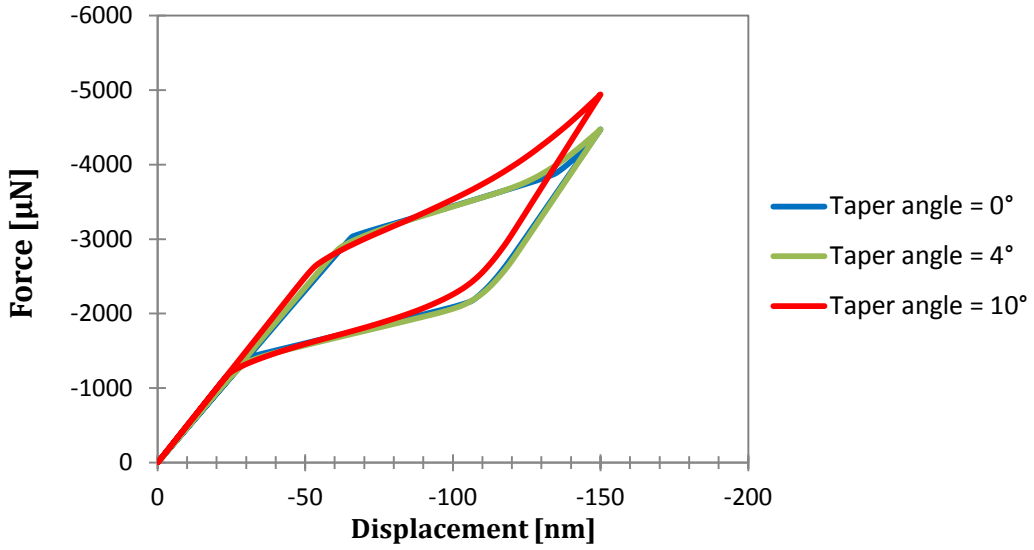

Fig. 23 Force vs. displacement for micro-pillars with average diameter of 2000 nm and aspect ratio of 1.5.

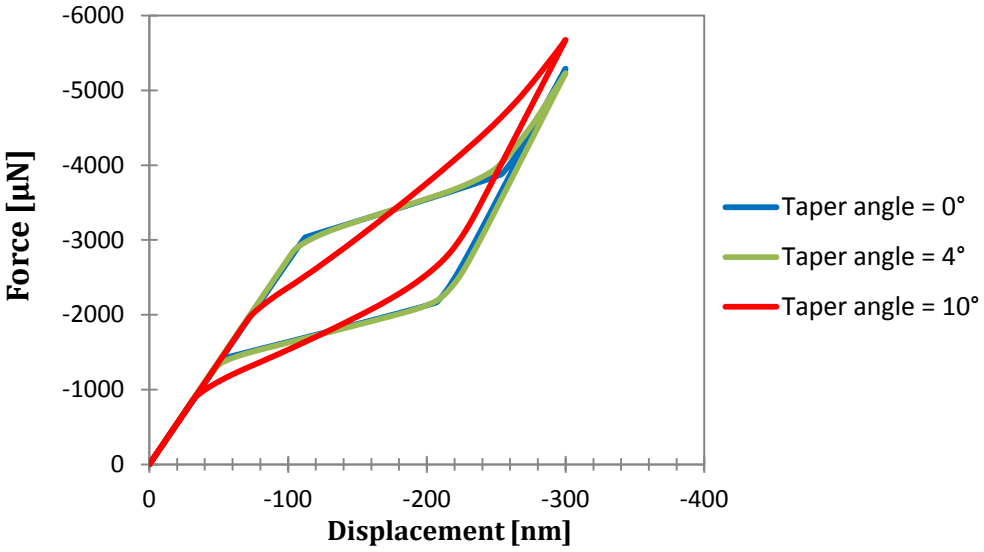

Fig. 24 Force vs. displacement for micro-pillars with average diameter of 2000 nm and aspect ratio of 3.

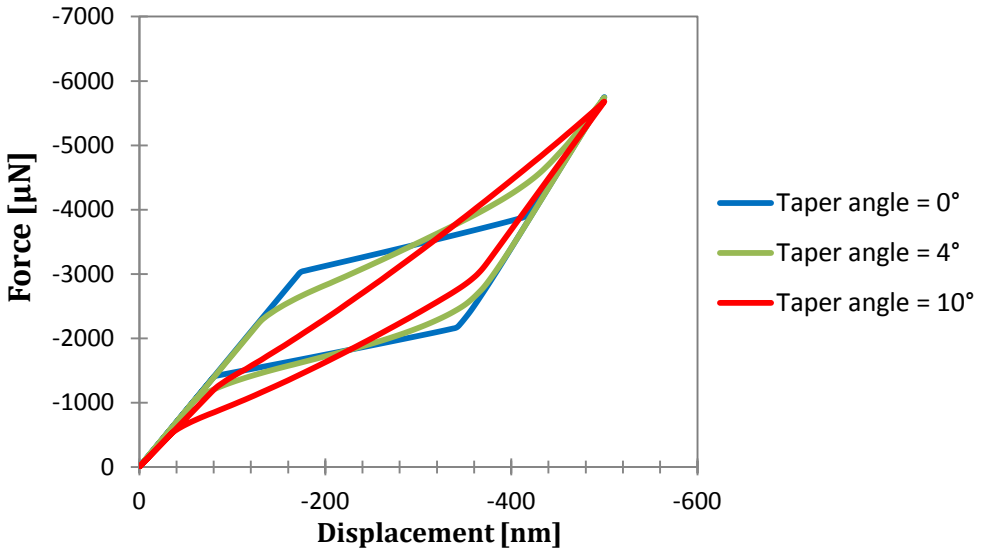

Fig. 25 Force vs. displacement for micro-pillars with average diameter of 2000 nm and aspect ratio of 5.

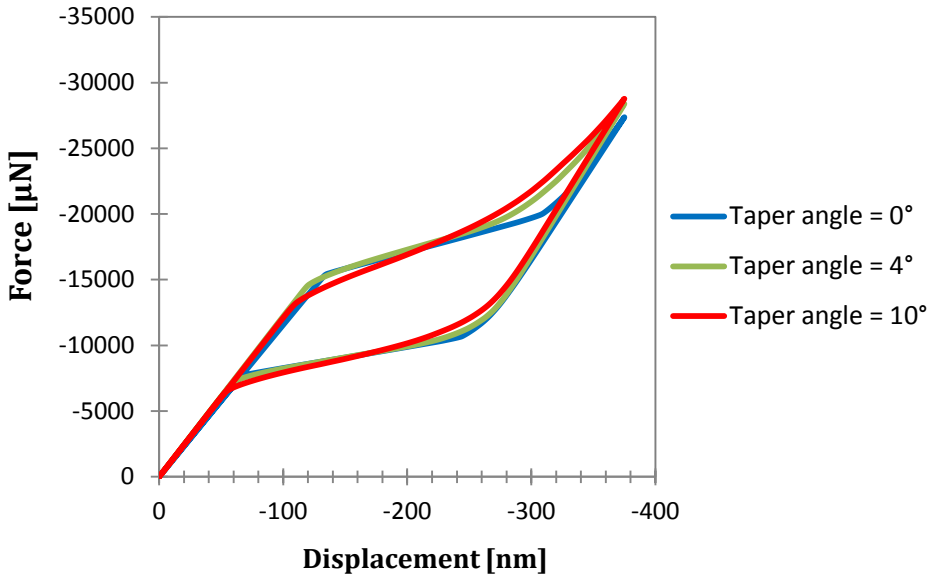

Fig. 26 Force vs. displacement for micro-pillars with average diameter of 5000 nm and aspect ratio of 1.5.

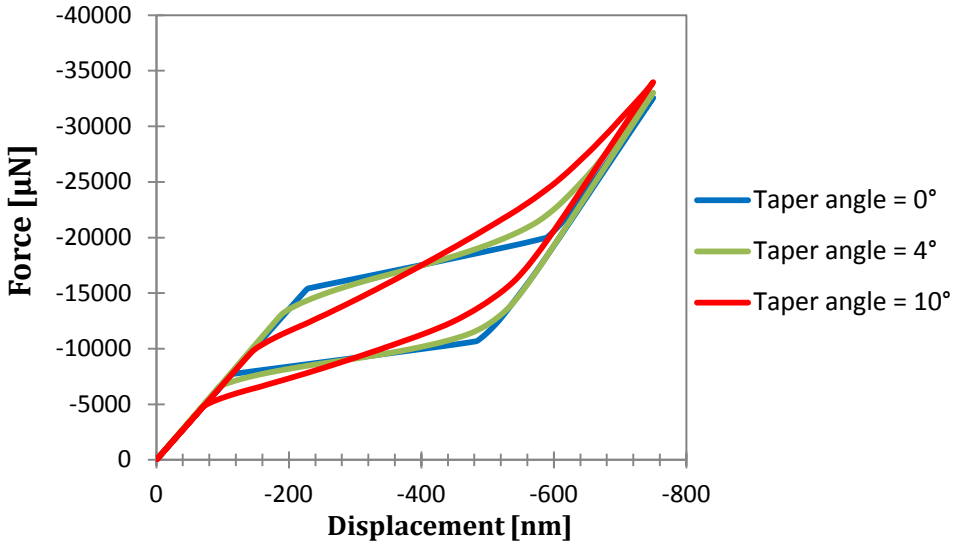

Fig. 27 Force vs. displacement for micro-pillars with average diameter of 5000 nm and aspect ratio of 3.

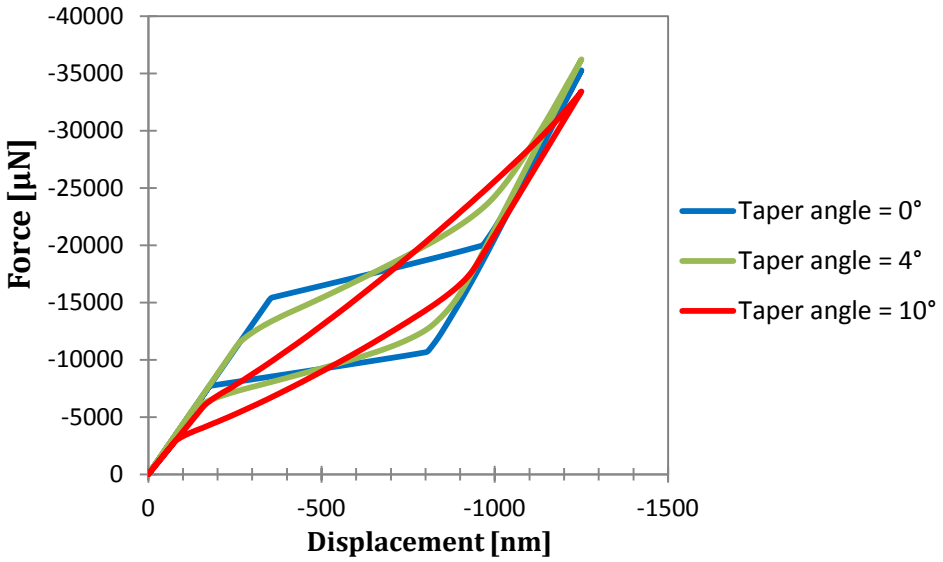

Fig. 28 Force vs. displacement for micro-pillars with average diameter of 5000 nm and aspect ratio of 5.

It is observed from the previous figures that the hysteresis of the micro-pillar response significantly decreases as the taper angle increases for pillars with high aspect ratios. This is due to a non-uniform stress distribution along the pillar, which results into non-uniform transformation along the pillar. Due to this non-uniform distribution, there are regions of the pillar that are fully austenite, fully martensite, and in transformation during most of the loading. The mixture of the austenite, martensite and transforming regions along the pillar creates an apparent force-displacement slope that does not correspond to the elastic modulus of any of the two phases. This force-displacement slope does not vary too much in a magnitude, making the force-displacement response closer to a straight line as the taper angle increases. Figure 29 show the martensite volume fraction for a micro-pillar of 500 nm diameter, aspect ratio of 5 and taper angle of 0 degrees. Figure 30 show the martensite volume fraction of a micro-pillar of 500 nm

diameter, aspect ratio of 5 and taper angle of 10 degrees. It should be noted that any regions with martensite volume fraction slightly greater than 1 or lower than 0 are due to slight numerical errors. Figures 29–30 show the conditions at maximum displacement (5%) of the pillar length.

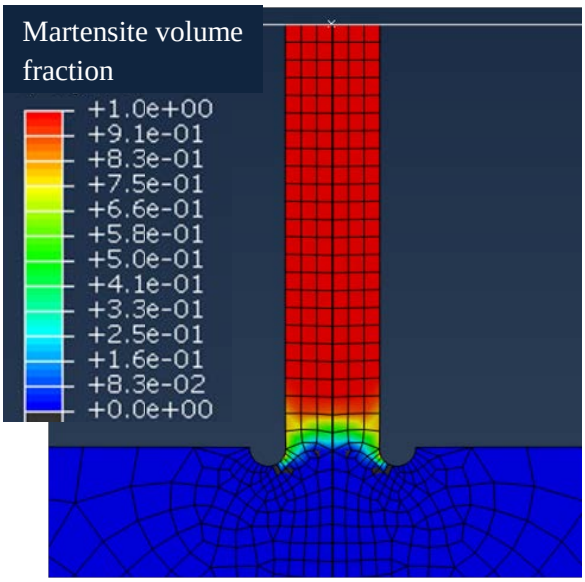

Fig. 29 Martensite volume fraction at maximum displacement of a micro-pillar of 500 nm average diameter, aspect ratio of 5, and taper angle of 0 degrees.

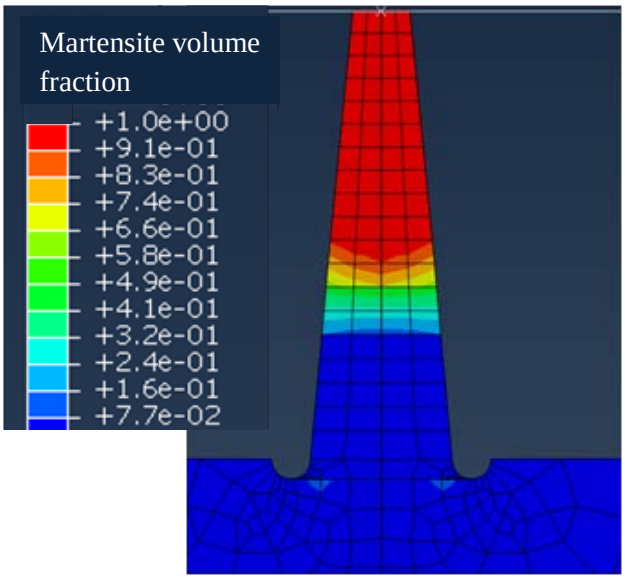

Fig. 30 Martensite volume fraction at maximum displacement of a micro-pillar of 500 nm average diameter, aspect ratio of 5, and taper angle of 10 degrees.

From the previous figures one can observe that the stress and martensite volume fraction are fairly uniform along most of the micro-pillar with zero degree taper angle. Figure 30 shows a region at the top of the pillar fully transformed to martensite, one region at the middle of the pillar in incomplete transformation, and a region at the bottom of the pillar fully austenite. As previously stated, this mixture of regions with different stiffness creates a force-displacement response with a slope that does not change in great magnitude during the entire loading. This causes the hysteresis to decrease. For pillars with low taper angle, the typical pseudoelastic response is observed and the loadings where most of the pillar experienced transformation were clearly identified.

The region at the top of the pillar has lower diameter that the bottom region therefore higher transformation stresses due to the size effect. Even though the regions of smaller

diameters experience higher stress than those of higher diameters, they may transform at about the same loading range of the regions of higher diameters since their transformation stresses are higher. This is why for pillars with low taper angles the force-displacement response is very similar to that of the zero taper angle pillars. However, for high taper angles where the stress distribution along the pillar is highly uneven, the transformation along the pillar occurs at different loadings regardless of the size effect. To illustrate this, Fig. 31 shows the comparison between the pseudoelastic response of pillars of 500 nm average diameter, aspect ratio of 5, and taper angle of 10°, one with sectioned region properties and the other with average diameter constant properties. Here, it is observable that their responses are almost the same. Figure 32 shows the martensite volume fraction of a micro-pillar of 500 nm diameter, aspect ratio of 5 and taper angle of 10° with constant average diameter properties along its length. Here, it is observable that the martensite volume fraction distribution of the micro-pillar with constant average diameter properties is very similar to that of the micro-pillar divided into sections presented in Fig. 30.

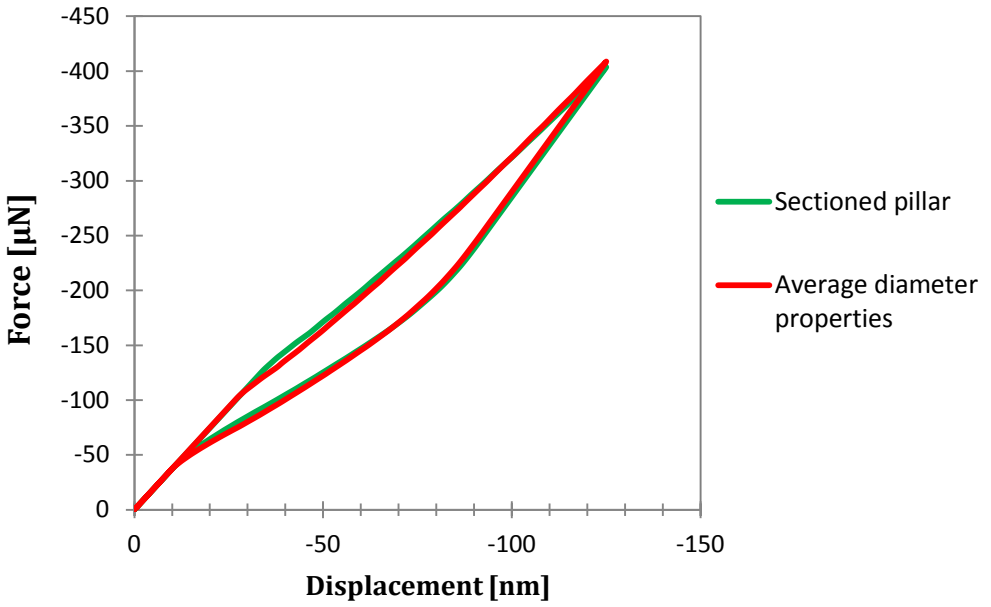

Fig. 31 Stress-strain behavior of micro-pillars of 500 nm average diameter, aspect ratio of 5, and taper angle of 10 degrees.

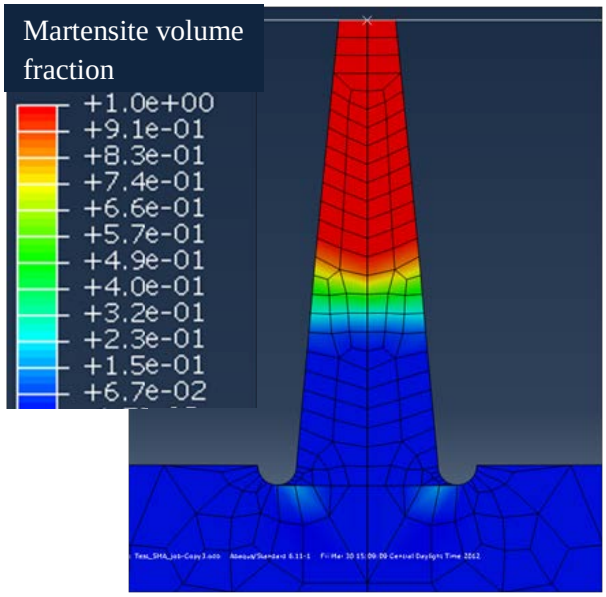

Fig. 32 Martensite volume fraction at maximum displacement of a micro-pillar of 500 nm average diameter, aspect ratio of 5, and taper angle of 10 degrees with average diameter properties along its length.

Figures 33–41 show the responses of micro-pillars with equal aspect ratio and taper angles but different average diameters. Here, the force-displacement data was converted into stress-strain using Eqs. (44) and (45).

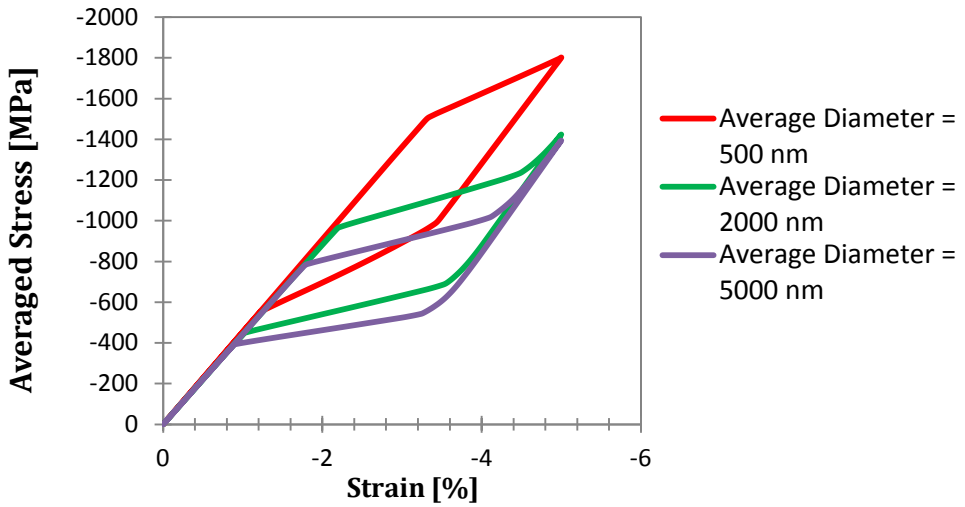

Fig. 33 Average stress vs. strain for micro-pillars with aspect ratio of 1.5 and taper angle of zero degrees.

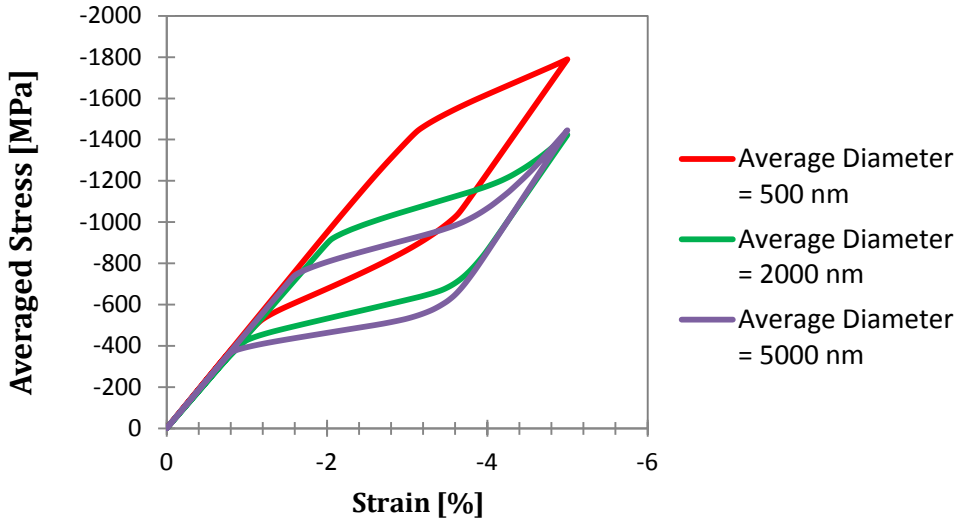

Fig. 34 Average stress vs. strain for micro-pillars with aspect ratio of 1.5 and taper angle of 4 degrees.

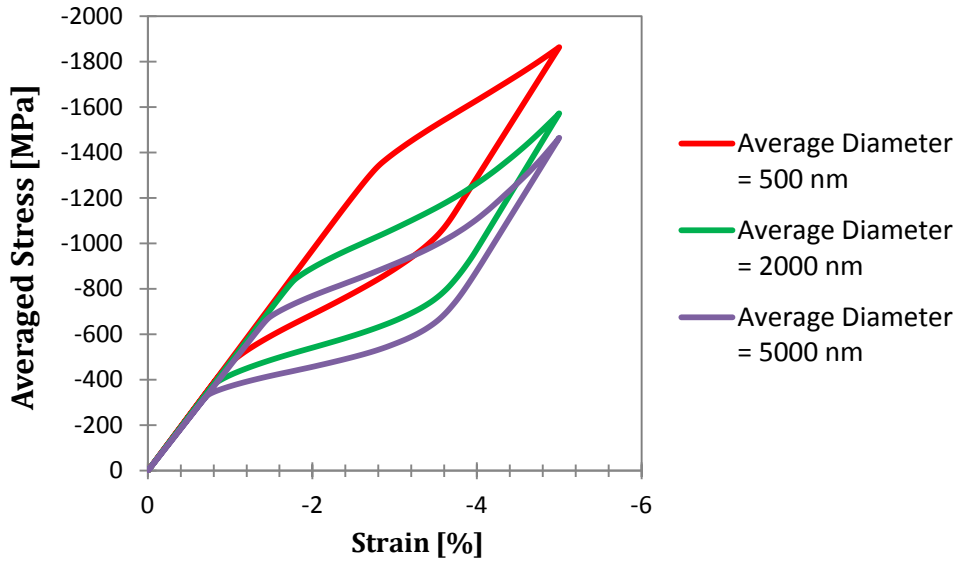

Fig. 35 Average stress vs. strain for micro-pillars with aspect ratio of 1.5 and taper angle of 10 degrees.

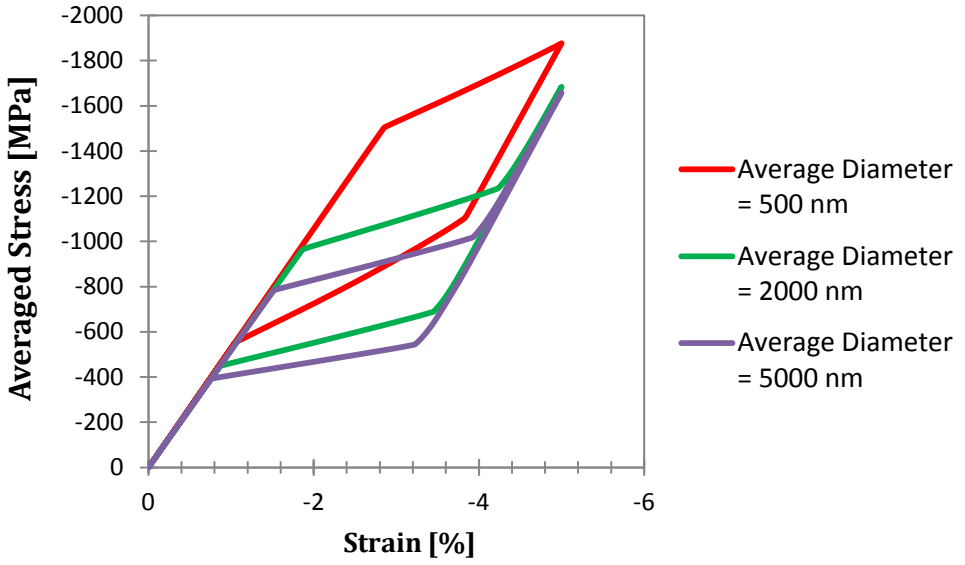

Fig. 36 Average stress vs. strain for micro-pillars with aspect ratio of 3 and taper angle of zero degrees.

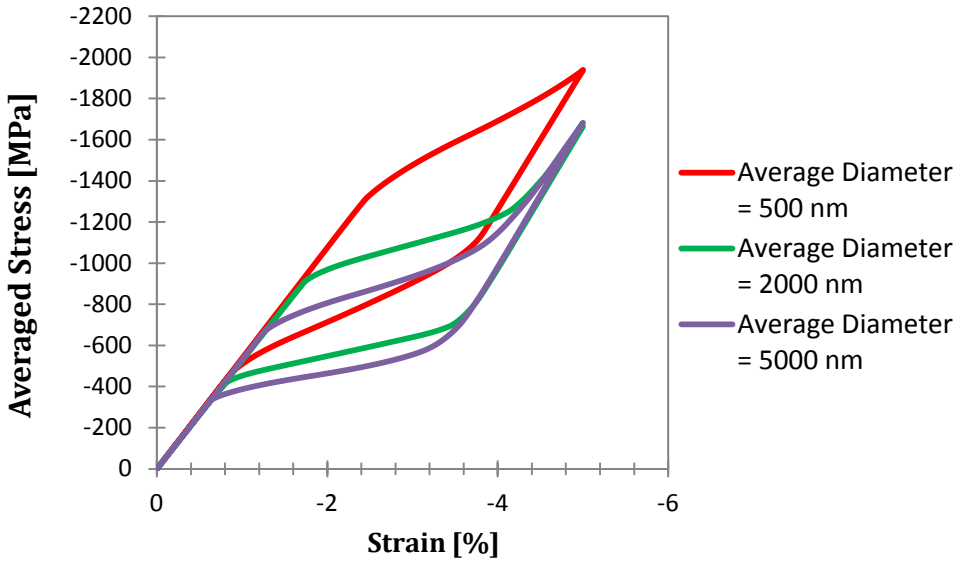

Fig. 37 Average stress vs. strain for micro-pillars with aspect ratio of 3 and taper angle of 4 degrees.

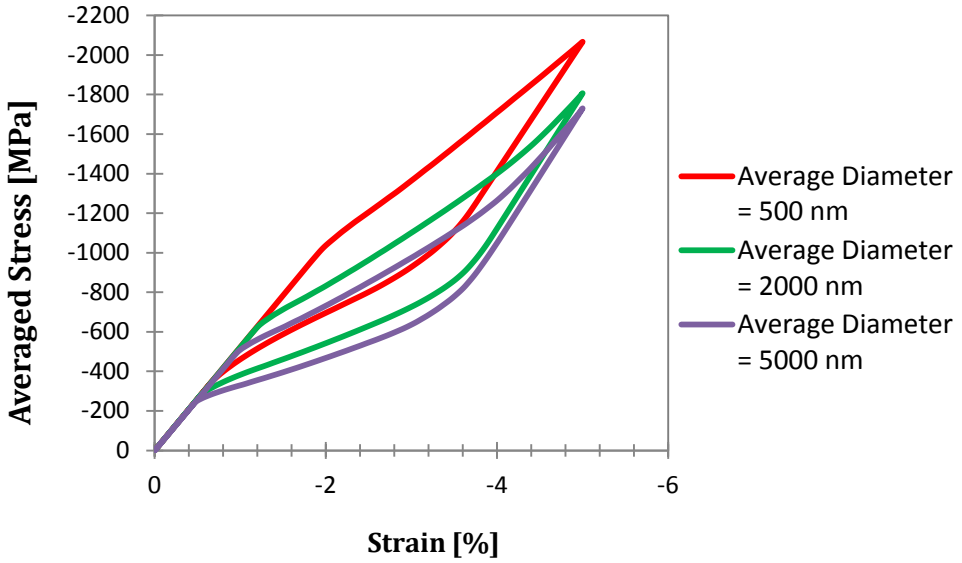

Fig. 38 Average stress vs. strain for micro-pillars with aspect ratio of 3 and taper angle of 10 degrees.

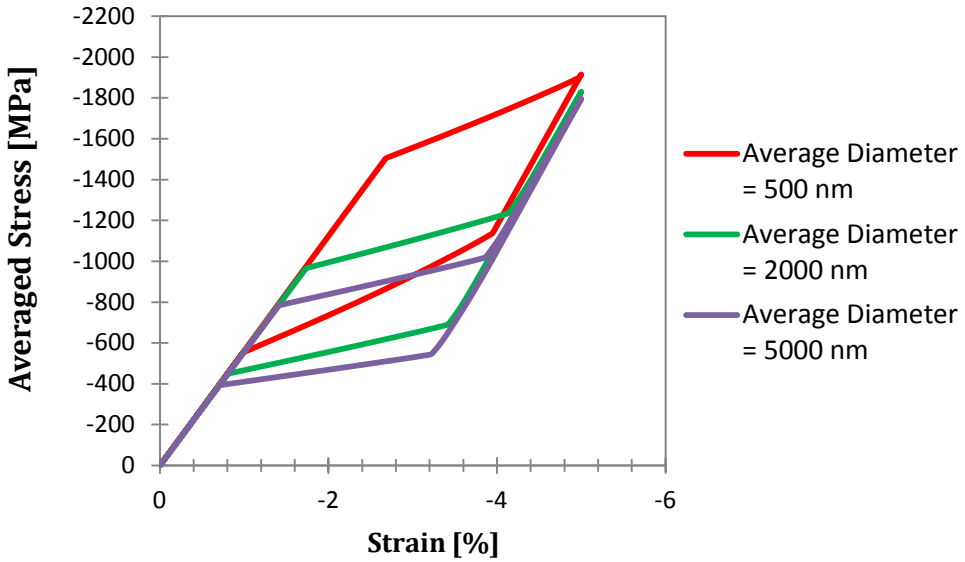

Fig. 39 Average stress vs. strain for micro-pillars with aspect ratio of 5 and taper angle of zero degrees.

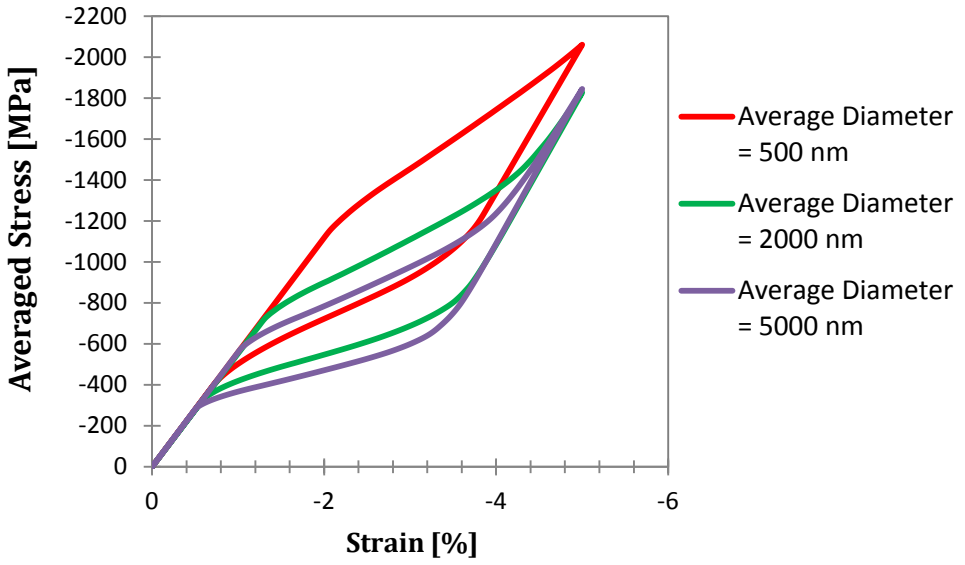

Fig. 40 Average stress vs. strain for micro-pillars with aspect ratio of 5 and taper angle of 4 degrees.

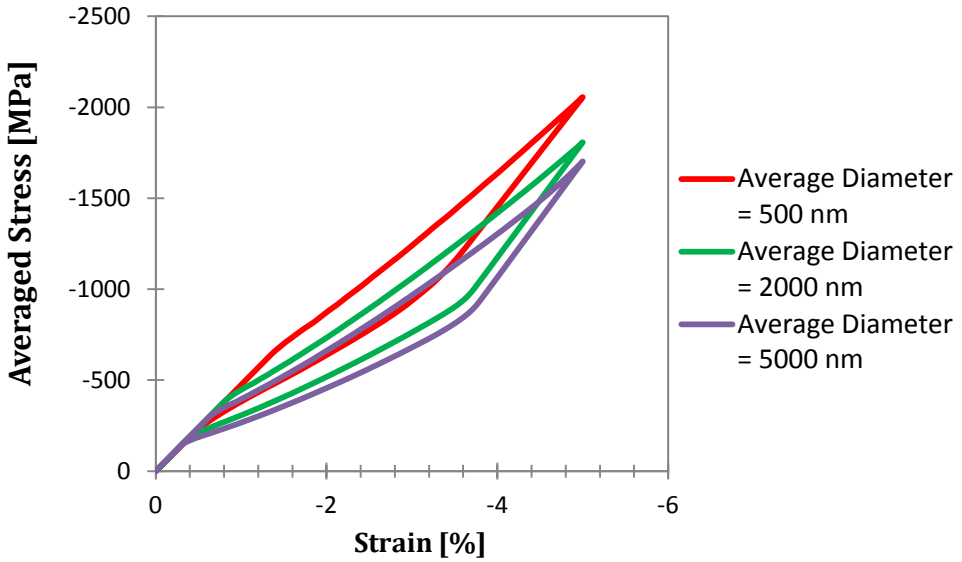

Fig. 41 Average stress vs. strain for micro-pillars with aspect ratio of 5 and taper angle of 10 degrees.

From the previous figures, one can observe the change in the pillar compression response for pillars of equal aspect ratio and taper angle but different average diameter. The differences from the responses of pillars of equal aspect ratio and taper angle are due to the size effect. In pillars with low aspect ratios and low taper angles the size effect on the transformation stresses is clearly revealed in the stress-strain response. For pillars with high aspect ratio and high taper angle the size effect does not significantly affect the stress-strain response of the micro-pillars, this case is clearly revealed by comparing Fig. 33 (micro-pillar with zero taper angle and aspect ratio of 1.5) and Fig. 41 (micro-pillar with taper angle of 10° and aspect ratio of 5). In Fig. 44 one can observe that the responses for pillars with average diameters of 500 nm, 2000 nm, and 5000 nm are very similar regardless of the size effect. Here, the stresses at the top of the micro-pillar were very high compared to the stresses at the bottom. Due to this unequal stress distribution,

the pillar does not transform uniformly. As previously stated, as the taper angle increases, the stress-strain response gets more similar to a line and it has a slope that does not vary excessively during the entire loading. This is why the differences in the responses do not seem to be significantly affected by the size effect.

CHAPTER IV

SUMMARY AND CONCLUSIONS

Isothermal compression experiments from literature of bulk and micro NiTi (50.9 at% Ni) pillars were analyzed to determine the critical transformation stresses for different pillar diameters. The analysis of experimental data shows that the transformation stresses increase as the micro-pillar average diameter decreases. The relations between the critical transformation stresses and the pillar diameter were modeled using power functions. It was assumed that the elastic modulus of the austenite and martensite phases, the transformation strain parameters, and stress influence coefficients are independent of the micro-pillar size. The model was implemented in ABAQUS using a user material subroutine. In the simulations, the tapered pillars were divided into ten sections along their long dimension. Each section was assigned with the transformation temperatures at zero stress corresponding to the average diameter of the section. A displacement of 5% the pillar length was applied at the top of the pillar in several steps, measuring reaction force for each step.

The proposed size effect captures well the micro-pillars pseudoelastic behavior. Comparisons between simulations and experiments show that the model accurately predicts the pseudoelastic response of bulk and micro-pillars. Parametric studies were performed to find the effects of taper angle and aspect ratio on the micro-pillars behavior. The results from the parametric studies show that the hysteresis of the

compression response decreases as the taper angle increases. The size effect of the micro-pillar diameter on their compression response is less significant for micro-pillars of higher aspect ratios and higher taper angles. This is due to a non-uniform stress distribution along the pillar, which results into non-uniform transformation along the pillar. Due to this non-uniform distribution, there are regions of the pillar that are fully austenite, fully martensite, and in transformation during most of the loading. The mixture of the austenite, martensite and transforming regions along the pillar creates an apparent force-displacement slope that does not correspond to the elastic modulus of any of the two phases. This force-displacement slope does not vary too much in a magnitude, making the force-displacement response closer to a straight line as the taper angle increases.

REFERENCES

[1] Phillips, F. R., Fang, D., Zheng, H., and Lagoudas, D. C., "Phase Transformation in Free-standing SMA Nanowires," *Acta Materialia*, Vol. 59, Issue. 5, 2011, pp. 1871–1880.

[2] Schwartz, M., *Smart Materials*, CRC Press, Boca Raton, FL, 2009.

[3] Lagoudas, D. C. (ed.), *Shape Memory Alloys: Modeling and Engineering Applications*, Springer, New York, 2008.

[4] Kahn, H., Huff, M. A., and Heuer, A. H., "The TiNi Shape-memory Alloy and its Applications for MEMS," *Journal of Micromechanics and Microengineering*, Vol. 8, No. 3, 1998, pp 213–221.

[5] Lee, A. P., Ciarlo, D. R., Krulevitch, P. A., Lehew, S., Trevino, J., and Northrup, M. A., "A Practical Microgripper by Fine Alignment, Eutectic Bonding and SMA Actuation," *Sensors and Actuators A: Physical*, Vol. 54, Issues 1–3,1996, pp. 755–759.

[6] Fu, Y., Du, H., Huang, W., Zhang, S., and Hu, M., "TiNi-based Thin Films in MEMS Applications: A Review," *Sensors and Actuators A: Physical*, Vol. 112, Issues 2–3, 2004, pp. 395–408.

[7] Krulevitch, P., Lee, A. P., Ramsey, P. B., Trevino, J. C., Hamilton, J., and Northrup, M. A., "Thin Film Shape Memory Alloy Microactuators," *Journal of Microelectromechanical Systems*, Vol. 5, Issue 4, 1996, pp. 270–282.

[8] Wolf, R. H., and Heuer, A. H., "TiNi (Shape Memory) Films Silicon for MEMS Applications," *Journal of Microelectromechanical Systems*, Vol. 4, Issue 4, 1995, pp. 206–212.

[9] Benard, W. L., Kahn, H., Heuer, A. H., and Huff, M. A., "Thin-film Shape-memory Alloy Actuated Micropumps," *Journal of Microelectromechanical Systems*, Vol. 7, Issue 2, 1998, pp. 245–251.

[10] Miyazaki, S., and Ishida, A., "Martensitic Transformation and Shape Memory Behavior in Sputter-deposited TiNi-based Thin Films," *Materials Science and Engineering: A*, Vols. 273–275., 1999, pp. 106–133.

[11] Ishida, A., Takei, A., and Miyazaki, S., "Shape Memory Thin Film of Ti-Ni Formed by Sputtering," *Thin Solid Films*, Vol. 228, Issues 1–2, 1993, pp. 210–214.

[12] Bhattacharya, K., and James, R. D., "The Material Is the Machine," *Science*, Vol. 307, No. 5706, 2005, pp. 53–54.

[13] Wang, Z. L., "Characterizing the Structure and Properties of Individual Wire-like Nanoentities," *Advanced Materials*, Vol. 12, No. 17, 2000, pp. 1295–1298.

[14] Wong, E. W., Sheehan, P. E., and Lieber, C. M., "Nanobeam Mechanics: Elasticity, Strength, and Toughness of Nanorods and Nanotubes," *Science*, Vol. 277, No. 5334, 1997, pp. 1971–1975.

[15] Li, X., Gao, H., Murphy, C. J., and Caswell, K. K., "Nanoindentation of Silver Nanowires," *Nano Letters*, Vol. 3, No. 11, pp. 1495–1498.

[16] Dou, R., and Derby, B., "The Strength of Gold Nanowire Forest," *Scripta Materialia*, Vol. 59, Issue 2, 2008, pp. 151–154.

[17] Wan, D., and Komvopoulos, K., "Thickness Effect on Thermally Induced Phase Transformations in Sputtered Titanium-nickel Shape-memory Films," *Journal of Materials Research*, Vol. 20, No. 6, 2005, pp. 1606–1612.

[18] Fu, Y. Q., Zhang, S., Wu, M. J., Huang, W. M., Du, H. J., Luo, J. K., Flewitt, A. J., and Milne, W. I., "On the Lower Thickness Boundary of Sputtered TiNi Films for Shape Memory Application," *Thin Solid Films*, Vol. 515, Issue 1, 2006, pp. 80–86.

[19] Waitz, T., Kazykhanov, V., and Karnthaler, H. P., "Martensitic Phase Transformations in Nanocrystalline NiTi Studied by TEM," *Acta Materialia*, Vol. 52, Issue 1, 2004, pp. 137–147.

[20] Waitz, T., Spisak, D., Hafner, J., and Karnthaler, H. P., "Size-dependent Martensitic Transformation Path Causing Atomic-scale Twinning of Nanocrystalline NiTi Shape Memory Alloys," *Europhysics Letters*, Vol. 71, No. 1, 2005, pp. 98–103.

[21] Busch, J. D., Johnson, A. D., Lee, C. H., and Stevenson D. A., "Shape-memory Properties in Ni-Ti Sputter-deposited Film," *Journal of Applied Physics*, Vol. 68, Issue 12, 1990, pp. 6224–6228.

[22] Ishida, A., and Sato, M., "Thickness Effect on Shape Memory Behavior of Ti-50.0at.%Ni Thin Film," *Acta Materialia*, Vol. 51, Issue 18, 2003, pp. 5571–5578.

[23] Glezer, A. M., Blinova, E. N., Pozdnyakov, V. A., and Shelyakov, A. V., "Martensite Transformation in Nanoparticles and Nanomaterials," *Journal of Nanoparticle Research*, Vol. 5, No. 5–6, 2003, pp. 551–560.

[24] Krulevitch, P., Ramsey, P. B., Makowiecki, D. M., Lee, A. P., Northrup, M. A., and Johnson, G. C., "Mixed-sputter Deposition of Ni-Ti-Cu Shape Memory Films," *Thin Solid Films*, Vol. 274, Issues 1–2, 1996, pp. 101–105.

[25] Frommen, C., Wilde, G., and Rösner, H., "Wet-chemical Synthesis and Martensitic Phase Transformation of Au-Cd Nanoparticles with Near-equiatomic Composition," *Journal of Alloys and Compounds*, Vol. 377, Issues 1–2, 2004, pp. 232–242.

[26] Fu, Y., and Shearwood, C., "Characterization of Nanocrystalline TiNi Powder," *Scripta Materialia*, Vol. 50, Issue 3, 2004, pp. 319–323.

[27] Frick, C. P., Clark, B. G., Orso, S., Sonnweber-Ribic, P., and Arzt, E., "Orientation-Independent Pseudoelasticity in Small-scale NiTi Compression Pillars," *Scripta Materialia*, Vol. 59, Issue 1, 2008, pp. 7–10.

[28] Frick, C. P., Orso, S., and Artz, E., "Loss of Pseudoelasticity in Nickel-titanium Sub-micron Compression Pillars," *Acta Materialia*, Vol. 55, Issue 11, 2007, pp. 3845–3855.

[29] San Juan, J., Nó, M. L., and Schuh, C. A., "Superelasticity and Shape Memory in Micro- and Nanometer-scale Pillars," *Advanced Materials*, Vol. 20, Issue 2, 2008, pp. 272–278.

[30] San Juan, J., Nó, M. L., and Schuh, C. A., "Nanoscale Shape-memory Alloys for Ultrahigh Mechanical Damping," *Nature Nanotechnology*, Vol. 4, 2009, pp. 415–419.

[31] Greer, J. R., "Effective Use of Focused Ion Beam (FIB) in Investigating Fundamental Mechanical Properties of Metals at the Sub-micron Scale," *MRS Proceedings*, 2006, pp. 983–990.

[32] Agrawal, R., Peng, B., Gdoutos, E. E., and Espinosa, H. D., "Elasticity Size Effects in ZnO Nanowires-A Combined Experimental-computational Approach," *Nano Letters*, Vol. 8, No. 11, 2008, pp. 3668–3674.

[33] Cuenot, S., Frétigny, C., Demoustier-Champagne, D., and Nysten, B., "Surface Tension Effect on the Mechanical Properties of Nanomaterials Measured by Atomic Force Microscopy," *Physical Review B*, Vol. 69, 2004, pp. 165410-1 – 165410-5.

[34] Stan, G., Ciobanu, C. V., Parthangal, P. M., and Cook, R. F., "Diameter-dependent Radial and Tangential Elastic Moduli of ZnO Nanowires," *Nano Letters*, Vol. 7, No. 12, 2007, pp. 3691–3697.

[35] San Juan, J., and Nó, M. L., "Superelasticity and Shape Memory at Nano-scale: Size Effects on the Martensitic Transformation," *Journal of Alloys and Compounds*, 2011, doi:10.1016/j.jallcom.2011.10.110.

[36] Greer, J. R., Oliver, W. C., and Nix, W. D., "Size Dependence of Mechanical Properties of Gold at the Micron Scale in the Absence of Strain Gradients," *Acta Materialia*, Vol. 53, Issue 6, 2005, pp. 1821–1830.

[37] Motz, C., Schöberl, T., and Pippan, R., "Mechanical Properties of Micro-sized Copper Bending Beams Machined by the Focused Ion Beam Technique," *Acta Materialia*, Vol. 53, Issue 15, 2005, pp. 4269–4279.

[38] Hutchinson, J. W., "Plasticity at the Micron Scale," *International Journal of Solids and Structures*, Vol. 37, Issues 1–2, 2000, pp. 225–238.

[39] Pellerin, J. G., Griffis, D. P., and Russell, P. E., "Focused Ion Beam Machining of Si, GaAs, and InP," *Journal of Vacuum Science & Technology B: Microelectronics and Nanometer Structures*, Vol. 8, Issue 6, 1990, pp. 1945–1950.

[40] Young, R. J., "Micro-machining Using a Focused Ion Beam," *Vacuum*, Vol. 44, Issues 3–4, 1993, pp. 353–356.

[41] Moghadam, S. H., Dinarvand, R., and Cartilier, L. H., "The Focused Ion Beam Technique: A Useful Tool for Pharmaceutical Characterization," *International Journal of Pharmaceutics*, Vol. 321, Issues 1–2, 2006, pp. 50–55.

[42] Reyntjens, S., and Puers, R., "A Review of Focused Ion Beam Applications in Microsystem Technology," *Journal of Micromechanics and Microengineering*, Vol. 11, No. 4, 2001, pp. 287–300.

[43] Russell, P. E., Stark, T. J., Griffis, D. P., Phillips, J. R., and Jarausch, K. F., "Chemically and Geometrically Enhanced Focused Ion Beam Micromachining," *Journal of Vacuum Science & Technology B*, Vol. 16, Issue 4, 1998, pp. 2494–2498.

[44] Picard, Y. N., Adams, D. P., Vasile, M. J., and Ritchey, M. B., "Focused Ion Beam-Shaped Microtools for Ultra-precision Machining of Cylindrical Components," *Precision Engineering*, Vol. 27, Issue 1, 2003, pp. 59–69.

[45] Morimoto, H., Sasaki, Y., Saitoh, K., Watakabe, Y., and Kato, T., "Focused Ion Beam Lithography and its Application to Submicron Devices," *Microelectronic Engineering*, Vol. 4, Issue 3, 1986, pp. 163–179.

[46] Langford, R. M., Nellen, P. M., Gierak, J., and Fu, Y., "Focused Ion Beam Micro- and Nanoengineering," *MRS Bulletin*, Vol. 32, 2007, pp. 417–423.

[47] Zhang, H., Schuster, B. E., Wei, Q., and Ramesh, K. T., "The Design of Accurate Micro-compression Experiments," *Scripta Materialia*, Vol. 54, Issue 2, 2006, pp. 181–186.

[48] Uchic, M. D., Dimiduk, D. M., Florando, J. N., and Nix W. D., "Sample Dimensions Influence Strength and Crystal Plasticity," *Science*, Vol. 305, No. 5686, 2004, pp. 986–989.

[49] Dimiduk, D. M., Uchic, M. D., and Parthasarathy, T. A., "Size-affected Single-slip Behavior of Pure Nickel Microcrystals," *Acta Materialia*, Vol. 53, Issue 15, 2005, pp. 4065–4077.

[50] Uchic, M. D., Dimiduk, D. M., Wheeler, R., Shade, P. A., and Fraser, H. L., "Application of Micro-sample Testing to Study Fundamental Aspects of Plastic Flow," *Scripta Materialia*, Vol. 54, Issue 5, 2006, pp. 759–764.

[51] Gall, K., Dunn, M. L., Liu, Y., Labossiere, P., Sehitoglu, H., and Chumlyakov, Y. I., "Micro and Macro Deformation of Single Crystal NiTi," *Journal of Engineering Materials and Technology*, Vol. 124, Issue 2, pp. 238–245.

[52] Gall, K., Tyber, J., Brice, V., Frick, C. P., Maier, H. J., and Morgan, N., "Tensile Deformation of NiTi Wires," *Journal of Biomedical Materials Research Part A*, Vol. 75A, Issue 4., 2005, pp. 810–823.

[53] Gall, K., and Maier, H. J., "Cyclic Deformation Mechanism in Precipitated NiTi Shape Memory Alloys," *Acta Materialia*, Vol. 50, 2002, pp. 4643–4657.

[54] Frick, C. P., Ortega, A. M., Tyber, J., Maksound, A. E. M., Maier, H. J., Liu, Y., and Gall, K., "Thermal Processing of Polycrystalline NiTi Shape Memory Alloys," *Materials Science and Engineering A*, Vol. 405, 2005, pp. 34–49.

[55] Boyd, J. G., and Lagoudas, D. C., "A Thermodynamical Constitutive Model for Shape Memory Materials. Part I. The Monolithic Shape Memory Alloy," *International Journal of Plasticity*, Vol. 12, Issue 6, 1996, pp. 805–842.

[56] Hartl, D. J., Lagoudas, D. C., and Calkins, F. T., "Advanced Methods for the Analysis, Design, and Optimization of SMA-based Aerostructures," *Smart Materials and Structures*, Vol. 20, No. 9, 2011, pp. 094006-1–094006-20.

[57] Lim, T. J., and McDowell, D. L., "Cyclic Thermomechanical Behavior of a Polycrystalline Pseudoelastic Shape Memory Alloy," *Journal of the Mechanics and Physics of Solids*, Vol. 50, Issue 3, 2002, pp. 651–676.

[58] Qidwai, M. A., Entchev, P. B., Lagoudas, D. C., and DeGiorgi, V. G., "Modeling of the Thermomechanical Behavior of Porous Shape Memory Alloys," *International Journal of Solids and Structures*, Vol. 38, Issues 48–49, 2001, pp. 8653–8671.

[59] Wang, X. M., Xu, B. X., and Yue, Z. F., "Micromechanical Modeling of the Effect of Plastic Deformation on the Mechanical Behaviour in Pseudoelastic Shape Memory Alloys," *International Journal of Plasticity*, Vol. 24, Issue 8, 2008, pp. 1307–1332.

CONTACT INFORMATION

Name:	Edwin Alexander Peraza Hernandez
Professional Address:	c/o Dr. Dimitris C. Lagoudas Texas A&M University Department of Aerospace Engineering 710 H. R. Bright Building 3141 TAMU College Station, TX 77843-3141
Email Address:	perazahernandez@gmail.com
Education:	B.S., Aerospace Engineering, Texas A&M University, December 2012 Summa Cum Laude Honors Undergraduate Research Fellow Tau Beta Pi Phi Kappa Phi Golden Key International Honour Society Sigma Gamma Tau Phi Eta Sigma